

Manuscript Number: JAES-D-13-00134R2

Title: The Large Aftershocks Triggered by the 2011 Mw 9.0 Tohoku-Oki Earthquake, Japan

Article Type: Research Article

Keywords: Tohoku-Oki earthquake, InSAR, slip distribution inversion, Coulomb stress change, aftershock triggering

Corresponding Author: Prof. Caijun XU, Ph.D.

Corresponding Author's Institution: Wuhan University

First Author: Ping He, Ph.D. Student

Order of Authors: Ping He, Ph.D. Student; Yangmao Wen, Ph.D.; Caijun XU, Ph.D.; Yang Liu, Ph.D.

Abstract: The Mw 9.0 Tohoku-Oki earthquake that occurred off the Pacific coast of Japan on March 11, 2011, was followed by thousands of aftershocks, both near the plate interface and in the crust of inland eastern Japan. In this paper, we report on two large, shallow crustal earthquakes that occurred near the Ibaraki-Fukushima prefecture border, where the background seismicity was low prior to the 2011 Tohoku-Oki earthquake. Using densely spaced geodetic observations (GPS and InSAR datasets), we found that two large aftershocks in the Iwaki and Kita-Ibarake regions (hereafter referred to as the Iwaki earthquake and the Kita-Ibarake earthquake) produced 2.1 m and 0.44 m of motion in the line-of-sight (LOS), respectively. The azimuth-offset method was used to obtain the preliminary location of the fault traces. The InSAR-based maximum offset and trace of the faults that produced the Iwaki earthquake are consistent with field observations. The fault location and geometry of these two earthquakes are constrained by a rectangular dislocation model in a multilayered elastic half-space, which indicates that the maximum slips for the two earthquakes are 3.28 m and 0.98 m, respectively. The Coulomb stress changes were calculated for the faults following the 2011 Mw 9.0 Tohoku-Oki earthquake based on the modeled slip along the fault planes. The resulting Coulomb stress changes indicate that the stresses on the faults increased by up to 1.1 MPa and 0.7 MPa in the Iwaki and Kita-Ibarake regions, respectively, suggesting that the Tohoku-Oki earthquake triggered the two aftershocks, supporting the results of seismic tomography.

## Covering Letter

Dear Editor,

My name is Caijun Xu, come from School of Geodesy and Geomatics, Wuhan University. I submit this manuscript named “The Large Aftershocks Triggered by the 2011 Mw 9.0 Tohoku-Oki Earthquake, Japan” to “Journal of Asian Earth Sciences” and waiting for reviewing by other scientists.

In this paper, the surface deformation and source parameters of two large aftershocks in Iwaki and Kita-Ibarake regions were extracted using geodetic data firstly. Then, the rectangle dislocation model in elastic half-space was used to derive the geometric and kinematic characteristic of aftershock faults. Lastly, the Coulomb stress changes on those fault planes caused by the 2011 Mw 9.0 earthquake are calculated basing on the inverted fault geometries. The results show that the seismogenic faults are nearly pure normal faulting, and the Coulomb stress changes increase with 1.1 MPa and 0.7 MPa, respectively in Iwaki and Kita-Ibarake regions, suggesting that the static Coulomb stress change induced by the Tohoku-Oki earthquake promote the two aftershocks triggered.

My email address is [cjxu@sgg.whu.edu.cn](mailto:cjxu@sgg.whu.edu.cn). Tel.:+86-27-68778805,

Fax:+86-27-68778371.

Best regards,

## Research Highlight

1. Derive the deformation for the large aftershocks in Iwaki and Kita-Ibarake region
2. Determine the fault trace from the azimuth offsets and InSAR
3. Provide the source mechanism of two large aftershocks inverted from the InSAR data
4. The Coulomb stress changes infer aftershocks triggered by the main event

## Responses to Reviewers for: Manuscript Number: JAES-D-13-00134

Ping He, Yangmao Wen, Caijun Xu\*, Yang Liu

Many thanks for the constructive comments to our paper! We provide a point-by-point response to Reviewers' comments in this response letter.

**Note:** Reviewers' comments are in "***bold italics***", and our responses in "regular" text for clarity. "*Italic regular*" text is extracted from the revised manuscript.

### Response to Reviewers

#### Reviewer #1 (Comments to Author):

*1. According to USGS, the Mj 7.0 Iwaki earthquake called in the manuscript consists, in fact, of at least 4 earthquakes of magnitude Mw5.5-6.6, which were occurred within the data acquisition period. Though it is difficult to separate the spatial distribution of deformation of these events by using the available geodetic data, it is important to mention the seismological observations. Additionally, it should be interesting to investigate possible interactions between these large aftershocks.*

**Ans:** Thank you for the valuable comments. The JMA earthquake catalog indicates that there were several Mw 5.5-6.6 earthquakes that occurred within the SAR data acquisition period (we plot the epicenters of these earthquakes in Fig. 1). It is indeed difficult to separate the spatial distributions of deformation caused by these events using the available geodetic data, but we used the deformation distribution in the interferogram in Fig. 2(a) to identify the most likely earthquake to have caused the deformation. In addition, small earthquakes (Mw<6.0) do not cause large surface ruptures in this region, so the deformation in T403 is mainly caused by the Mj 7.0 Iwaki earthquake. We then referred to the seismological observations and added the above explanation to the paper. The interaction of these large aftershocks is an interesting question, and it may be the next stage of this work.

*2. In Fig. 6, the Coulomb stress changes were calculated on receiver faults parallel to the main fault and on optimally oriented planes. Here the optimally oriented plane is derived using the approach proposed by Xu et al. (2009). In fact, for any spatial location there should be two conjugate fault planes, on which the Coulomb stress associated with the given stress tensor takes the same maximum value. According to the definition by Xu et al. (2009), both of the conjugate fault planes can be called the optimally oriented plane. As the stress tensor of the triggering earthquake varies in space, the optimally oriented plane varies in space, too. Moreover, the so-called optimal Coulomb stress should be positive overall according to the Xu et al. (2009) definition. In Fig. 6, however, the optimally oriented plane is fixed spatially (Strike/Dip/Rake = 20°/90°/85°) and the optimal Coulomb stress appears with both positive and negative values. Why?*

**Ans:** Thank you for your insightful comments on optimally oriented planes (OOPs). There are generally two types of receiver faults used for calculating Coulomb stress changes. One is a predefined receiver fault, and the other is an OOP. We employed the former type of receiver fault, i.e., with the fixed strike, dip and rake used by Toda (<http://www.usgsprojects.org/TohokuQuake2011/>). For OOPs, Xu et al. (2010) presented a concise formula to calculate OOPs and the Coulomb stress changes on them. Before using this formula, two aspects should be considered: the OOP should be determined using a known regional stress and it should be constrained by searching strikes, dips and rakes from given a parameter space of the receiver fault. In this formula, it is implied that a regional stress could be added into corresponding components of the stress tensor induced by an earthquake, allowing the OOP to be determined. The given parameter space is determined by the geological structure, as performed by McCloskey et al. (2003), which is used for calculating the Coulomb stress on an OOP. At least one of these two aspects must be carefully considered to determine the Coulomb stress on an OOP. Otherwise, as you stated, the Coulomb stress on an OOP would always be positive. In McCloskey et al. (2003), they considered the second aspect because the regional stress was not well constrained. They clearly present these two aspects of the formula and discuss additional aspects of it in an ongoing manuscript.

*3. The authors should cite the original references. For example, “Coulomb Failure Criterion is*

*the core of Coulomb stress triggering hypothesis, and the Coulomb stress change could be defined as  $\Delta CFF = \Delta\tau + \mu\Delta\sigma$  (Toda et al., 2011), where ...” in Line 244-246. Toda et al. (2011) is surely not the original source for the Coulomb stress definition.*

**Ans:** This mistake has been corrected by now referring to King et al. (1994).

**4. The English needs to be improved overall.**

**Ans:** We have revised our manuscript to improve our usage of English.

**Reviewer#2 (Comments to Author):**

*The paper is comprehensive and meaningful. It is valuable for publish. There are minor changes as following*

*1. p3, line 32, should be fault slip distribution;*

**Ans:** It have been changed by fault slip distribution

*2. p4, line 54, name of the fault should be given;*

**Ans:** There have been given the faults name for Iwake and Kita-Ibarake fault

*3. p4, line 54 to line 56, is not relevant;*

**Ans:** The sentence from line 54 to line 56 have been deleted

*4. p7, line 116, a reference is suggested for using polynomial method;*

**Ans:** The orbit error remove method for using polynomial has given the reference for Hanssen (2001)

*5. p10, line 192, dip angle should be rake angle;*

**Ans:** It has been revised.

*6. p12, line 228, resultto should be result to;*

**Ans:** The “resultto” is a writing error and have been changed by “result to”.

*7. p13, line 259, should be depth of aftershocks less than...;*

**Ans:** The “lower than” have been changed by “less than”.

*8. p15, line 305, should be source parameters.*

**Ans:** It have been changed

**Reviewer#3 (Comments to Author):**

*This paper attempts to determine the source parameters of two large aftershocks after the 2011 Mw 9.0 Tohoku-Oki Earthquake using geodetic observations and then assess whether they were triggered by the main shock, which is of interest for many readers.*

*The structure of this paper is appropriate, and English is generally ok.*

*I have only one very minor comment:*

*Geological background. This section is a bit weak. More information on tectonic background is desirable.*

**Ans:** Thank you for your significant comments. We have added more information on tectonic about our testing region such as “*Western Iwaki city of Abukuma-sanchi is the focal region. Metamorphic rocks and Cretaceous strata, granite and epidiorite are distributed in this area, and also the fore-arc deposit with unconformity in Tertiary is distributed (Kubo et al. 2007).*” “*For the Mj 7.0 earthquake there produced a 14-km-long westward normal-slip rupture on the Itozawa fault and a 16-km-long southward normal-slip rupture on the Yunodake fault, and the northwest end of the rupture on the Yunodake fault is located ~2.5 km from that of the northwestern end of the Itozawa (Mizoguchi et al., 2012).*” and so on.

## Responses to Reviewers for: Manuscript Number: JAES-D-13-00134

Ping He, Yangmao Wen, Caijun Xu\*, Yang Liu

Many thanks for the constructive comments to our paper! We provide a point-by-point response to Editor's comments in this response letter.

**Note:** Editor's comments are in "*bold italics*", and our responses in "regular" text for clarity. "*Italic regular*" text is extracted from the revised manuscript.

### Response to Editor

#### Reviewer #1 (Comments to Author):

*1. Editor's comments: The authors have revised the manuscript reasonably well following the review comments. However, this paper should be further improved by adding more discussions on the crustal and upper mantle structure of the NE Japan arc and its relationship to the subduction dynamics and seismogenesis of the interplate megathrust zone. The following well-related papers should be cited and discussed for this purpose:*

*Zhao, D., Z. Wang, N. Umino, A. Hasegawa (2009) Mapping the mantle wedge and interplate thrust zone of the northeast Japan arc. Tectonophysics 467, 89-106.*

*Zhao, D., Z. Huang, N. Umino, A. Hasegawa, H. Kanamori (2011) Structural heterogeneity in the megathrust zone and mechanism of the 2011 Tohoku-oki earthquake (Mw 9.0). Geophys. Res. Lett. 38, L17308.*

*Huang, Z., D. Zhao (2013) Mechanism of the 2011 Tohoku-oki earthquake (Mw 9.0) and tsunami: Insight from seismic tomography. J. Asian Earth Sci. 70, 160-168.*

**Ans:** Thank you for your insightful comments on the discussion for the subduction dynamics and seismogenesis of the interplate megathrust zone in our paper, and this discussion is very important for our paper. In this revised manuscript, it is stated as follows:

*"For the northeast Japan arc, there exhibit strong lateral heterogeneity under the forearc region and a clear correlation between the structural heterogeneity and distribution of large earthquakes*

*occurred in the interplate thrust zone (Zhao et al., 2009). The Mw 9.0 Tohoku-Oki earthquake occurred in the interplate thrust zone and extends with large coseismic slip in a prominent high-V area, that all stress accumulated on the mainshock asperity may be released in a short time (Huang and Zhao, 2013) and influenced the tectonic stress field throughout Japan, particularly in northeastern Japan. The subducting Pacific plate and the overriding continental plate may become weakly coupled (Zhao et al., 2011). Zhao et al (2011) and Tong et al. (2012) used P- and S-wave data to obtain high-resolution tomographic images for the 2011 Iwaki earthquake (Mj 7.0) and for the area of the Fukushima nuclear power plant, their results exhibit that our study area with a high-velocity in the megathrust.”*



23 static Coulomb stress change induced by the Tohoku-Oki earthquake promote the two  
24 aftershocks triggered.

25 **Key words:** Tohoku-Oki earthquake, InSAR, slip distribution inversion, Coulomb  
26 stress change, aftershock triggering

27 **1. Introduction**

28 The Mw 9.0 Tohoku-Oki earthquake (USGS 38.322°N, 142.369°E) occurred on  
29 March 11, 2011 in the eastern Ocean of Japan (Fig. 1(a)), where the Pacific plate  
30 subducts beneath Honshu at a converge rate of ~9 cm/yr (Imanishi et al., 2012). Due to  
31 the release of long term stress accumulation, it generated tsunamis that cause  
32 significant locally in Sendai. Several estimates of slip distribution have been published  
33 (e.g., Fujii et al., 2011; Loveless and Meade, 2011; Yoshida et al., 2012), with a  
34 coseismic slip exceeded 30 m over a wide region.

35 The Tohoku-Oki earthquake has caused large variations in stress field not only  
36 near the source zone but also in regions far away from the epicenter, and so the  
37 seismic activity in the crust of the overriding plate west of the source area has  
38 increased significantly after the Tohoku-Oki earthquake (Okada et al., 2011).  
39 Thousands of aftershocks occurred during the first few months following the  
40 Tohoku-Oki earthquake. The Iwaki earthquake (Mj 7.0) occurred in a previous  
41 seismicity gap on 11 April 2011 and the Kita-Ibarake earthquake (Mj 6.0) occurred on  
42 19 March 2011, these were two of the major aftershocks following the Tohoku-Oki  
43 mainshock and the Iwaki earthquake was the strongest one hit the Japan land area  
44 (Note: Mj is the quick response report and CMT is the artificial post-processing report  
45 from Japan Meteorological Agency (JMA), both of the two report published by the  
46 NEID organization (<http://www.fnet.bosai.go.jp/event/search.php?LANG=en>)). For  
47 these two large aftershocks, there are at least two questions need to be answered. One  
48 question is the focal mechanism solution. In the previous published results, beside the

49 CMT solution from the NEID, there is little information about the slip distribution.  
50 Kobayashi et al (2011) have used InSAR data to detecte the Kita-Ibarake aftershock  
51 only. The other question is whether the two events were promoted by the Tohoku-Oki  
52 earthquake. Using the earthquake catalog data from the JMA (2004), some scholars (e.  
53 g., Okada et al., 2011; Toda et al., 2011; Imanishi et al, 2012) have calculated the  
54 Coulomb stress change on the fault nodal plane. Because of no detailed mechanism  
55 solution and slip distribution for these aftershocks, they could only get imprecise  
56 Coulomb stress value on the whole fault plane.

57 In this paper, geodetic data (GPS and InSAR data set) were used to constrain the  
58 location, geometry and slip distribution of the two events. After that whether these  
59 ruptures were promoted by the Tohoku-Oki earthquake is tested.

## 60 **2. Geological background**

61 As a plate collision junction region, the frequency of seismic activity is very high  
62 in Japan. The occurrence of Tohoku-Oki Mw 9.0 event influenced the tectonic stress  
63 field throughout Japan, particularly in northeast Japan, and several earthquakes with a  
64 magnitude 6 or larger occurred inland and off the coast in the Japan Sea (Hirose et al.,  
65 2011). Among these aftershocks, there are a Mj 7.0 earthquake on April 11 and 9  
66 moderate-magnitude earthquake ( $M_j \geq 5.0$ ) since April 18, 2011. Based on the seismic  
67 wave data, the focal mechanisms of the main aftershock in the testing region from  
68 JMA indicate that these events are normal faulting. From the statistics of aftershocks  
69 depth (Fig. 1(c) and (e)), it indicates that most of those aftershocks occurred in a depth  
70 lower than 20 km and were shallow earthquakes. However, the studied region has

71 lower background seismicity before the 2011 Tohoku-Oki earthquake (Imanishi et al.,  
72 2012).

73 In the Iwaki region, previous field investigation indicated that there existed active  
74 strike-slip and normal-faulting faults which were the Itozawa fault and Yunotake fault  
75 with general attitudes of strike N10°W, dip 70°W and strike N60°W dip 60°S,  
76 respectively (Active Fault and Earthquake Research Center, 2011). And both of the  
77 faults were ruptured during the Mj 7.0 earthquake and their surface ruptures were  
78 made up of normal faults scarps with offsets of up to 2 m (e.g., Otsubo et al., 2012).  
79 This feature revealed by the normal-faulting earthquakes was inconsistent with the  
80 present-day overall stress field in northeast Japan, which was characterized by a  
81 reverse-faulting regime with E-W compression (e.g., Zoback, 1992; Kubo et al., 2002;  
82 Townend and Zoback, 2006). In the northern Kita-Ibarake region, the seismicity  
83 drastically changed from a quiescent stage to an active stage, and no active fault was  
84 known.

### 85 **3. InSAR Surface displacements and Fault Characteristics**

#### 86 *3.1 InSAR analysis*

87 Phased Array type L-band Synthetic Aperture Radar (PALSAR) images from  
88 Advanced Land Observing Satellite (ALOS) were selected to derive the crustal  
89 deformation field for the testing region: Iwaki and Kita-Ibarake region respectively  
90 (Fig. 1(a)). During the PALSAR data acquisition time, the spatial distributions of  
91 aftershock in testing region are shown in Fig. 1(b) and (d). Also, the occurring time for  
92 the earthquakes whose magnitude >Mj 5.0 is shown in Fig. 1(b) and 1(d) and there

93 was no large earthquake ( $>M_j 5.0$ ) occurred before the Mw 9.0 Tohoku-Oki event. The  
94 depths of earthquakes were concentrated in range 2–16 km as in Fig. 1(c) and (e).

95 There were two interferometric pairs constructed from PALSAR data (Tab. 1).  
96 The SAR data were processed from raw products with the conventional two-pass  
97 differential interferometry approach (Massonnet et al., 1993) using the GAMMA  
98 software package (Werner et al., 2000). To ensure a high Signal Noise Ratio (SNR), a  
99 3:8 multi-look ratio was applied for the PALSAR data in the azimuth and the range  
100 directions during the processing. The 3-arc second SRTM DEM (Farr et al., 2007) is  
101 used to remove the phase component contributed by the topography. In order to further  
102 reduce the phase noise and improve the interferogram quality, a power spectrum filter  
103 (Goldstein et al., 1998) was applied to filter the interferograms. Then the  
104 minimum-cost flow algorithm (Chen and Zebker, 2001) was adopted to unwrap the  
105 differential interferograms. The geocoded interferograms were shown in the Fig. 2(a)  
106 and Fig. 2(d) (one fringe represents 11.8 cm deformation in all the interferograms). In  
107 the Fig. 2(a) and Fig. 2(d), there were very dense fringes in the interferograms; there  
108 are nearly 20 fringes in Fig. 2(a) and nearly 10 fringes in Fig. 2(d).

109 The contributions of interferogram (Fig. 2(a) and (d)) include the Mw 9.0  
110 coseismic deformation, large aftershock deformation, orbital error, atmosphere delays  
111 and topographic error phase. The atmospheric delays and topographic error phase are  
112 considered relatively small compared with the deformation (e. g., Feng et al., 2011),  
113 which will not be considered further in this study. The phase contributions can be  
114 expressed as follow:

115 
$$d_{insar} = d_{Mw9.0} + d_{orbit} + d_{deformation} + d_{error} \quad (1)$$

116 Where  $d_{orbit}$  is orbit error and can be removed by polynomial method.  $d_{Mw9.0}$  and  
 117  $d_{deformation}$  are coseismic and aftershock deformation respectively,  $d_{error}$  is the white  
 118 noise. Using the high dense GPS coseismic deformation observations we can  
 119 interpolate to obtain the InSAR coseismic deformation  $d_{Mw9.0}$ . Thus, the formula (1)  
 120 can be rewritten as follow:

121 
$$d_{deformation} = d_{insar} - d_{orbit} - d_{Mw9.0} - d_{noise} \quad (2)$$

122 After removing the  $d_{Mw9.0}$  deformation the corrected interferograms are shown in Fig.  
 123 2 (b) and (e). From the corrected interferogram in Fig. 2(b), it was found that the  
 124 maximum displacement was up to 2.1 m in line of sight (LOS) range. Our results  
 125 consistent with the field surveys which show that the Iwaki earthquake caused several  
 126 normal fault surface ruptured and the biggest deformation was up to 2 m (Otsubo et al.,  
 127 2012). From the corrected interferogram Fig. 2(e), it was found that the maximum  
 128 deformation in LOS range was 0.44 m in good agreement with ~0.4 m from previous  
 129 InSAR study (e. g., Kobayashi, 2011).

130 *3.2 Azimuth offsets*

131 In addition to phase information, SAR image also contains amplitude information  
 132 which is the function of image backscattering intensity. Deviation between the surface  
 133 deformation and satellite orbit as well as the difference of the amplitude of SAR image  
 134 before and after earthquake suggests that each pixel has an offset in azimuth and range  
 135 direction, respectively. For the earthquake in the remote region and a large number of  
 136 aftershocks after a mainshock, it is difficult to get the accurate surface rupture from

137 field surveys (Simons et al., 2002), but the azimuth offsets can easily determine the  
138 surface trace of seismogenic fault. In this study, the azimuth offsets were calculated by  
139 two accurate registration images along the orbit direction deviation. Azimuth offset  
140 accuracy is lower than phase observation, and the mean of azimuth offset is less  
141 sensitive to the surface deformation than coherent coefficient, Therefore, even in  
142 incoherent region (such as the high deformation gradient zone near fault) it can get  
143 high-quality azimuth offsets. Normally, the azimuth offsets can provide clear location  
144 of fault trace. The azimuth offsets of the interference pairs T403 and T404 are shown  
145 in Fig. 2(c) and (f).

146 As shown in Fig. 2(c), red solid line expressed the two faults namely Itozawa and  
147 Yunotake fault, respectively (Active Fault and Earthquake Research Center, 2011),  
148 where the green solid line expressed the corresponding faults trace extracted by  
149 azimuth offsets. Comparison of fault trace between geological field investigation (red  
150 line) and azimuth offsets (green line) shows the Yunotake fault trace has a well  
151 consistency, beside a whole shift the Itozawa fault trace has the same direction and  
152 length between them. Integrating with the pattern of interferogram, the fault trace  
153 extracted by azimuth offsets (green line) could be more reasonable. The strike  
154 direction and location of Itozawa and Yunotake fault can be determined by the azimuth  
155 offset method (Tab. 2).

156 As shown in Fig. 2(f), the fault trace cannot be identified by azimuth offsets in  
157 T404 interferogram pair, also there was no corresponding seismogenic fault detected  
158 by field survey results (JMA, 2004). We concluded that the seismogenic fault of this

159 event was a blind fault.

#### 160 **4. Fault Parameters Modeling**

161 Using the InSAR observations (Fig. 2(b) and (e)), we inverted the geometry  
162 parameter and slip distribution for seismogenic fault of aftershocks. In order to  
163 accelerate the inversion procedure, the interferograms were down-sampled to obtain a  
164 manageable data set with appropriate size, and then the rectangle dislocation model in  
165 elastic half-space was adopted for inversion.

##### 166 *4.1 Uniform-Slip Model*

167 To determine the source mechanism for the aftershocks, InSAR data sets were  
168 modeled with uniform slip on a rectangle dislocation in an elastic half-space (Okada,  
169 1985). Nine fault parameters (including longitude, latitude, length, minimum and  
170 maximum depth, strike, dip, slip and rake) were determined in this inversion  
171 procedure, which minimizes the misfit between the observations and predicted values  
172 using a non-linear, downhill simplex algorithm with multiple Monte Carlo restarts to  
173 avoid local minima (Clarke et al., 1997; Wright et al., 1999). Although the InSAR data  
174 is processed with the precise orbit information, interferogram still contained residual  
175 orbit error, so a linear function was applied in the inversion model to estimate the  
176 residual orbit error. The inverted model can be written as follow:

$$177 \quad d_{InSAR} = Gm + \varepsilon \quad (3)$$

178 Where  $d_{InSAR}$  is the InSAR observations,  $G$  is design matrix,  $m$  is parameter data  
179 set including fault parameters and orbit parameters, and  $\varepsilon$  is observation noise. The  
180 ultimate goal for inversion is to make observation data and model have a best fit, so as

181 to achieve the minimum objective function.

182 For the Iwaki earthquake, a two fault model was used to inverse the source  
183 mechanism. From the azimuth offsets and geological survey, the two fault location and  
184 strike angle were fixed. The inverted fault parameters are document in Tab. 2. The two  
185 faults of Itozawa and Yunotake fault were normal fault with dip angle of  $88.4^\circ$  and  
186  $73.5^\circ$ , respectively. The two seismogenic faults were mainly dip-slip with a small  
187 amount of strike-slip, and the total seismic moment was  $1.673 \times 10^{19}$  N m (Mw 6.75).  
188 Compared with the CMT result, the dip angle and rake angle are close, but the seismic  
189 moment was slightly larger in InSAR result.

190 For the Kita-Ibarake earthquake, one fault model was used to invert the source  
191 mechanism. The strike angle was fixed to  $155^\circ$  basing on the pattern of interferogram  
192 and the inverted fault parameters are shown in the Tab. 2. The dip angle is  $103.2^\circ$ ,  
193 nearly normal fault; seismogenic fault was characterized by significant dip-slip with a  
194 small amount of strike-slip. The fault which buried under the surface with the  
195 minimum depth was 1.96 km can be called as a blind fault, and it caused smaller  
196 deformation on the surface with no obvious azimuth offsets in Fig. 2(f). The seismic  
197 moment was  $2.28 \times 10^{18}$  N m (Mw 6.17). The dip angle was closed the CMT solution  
198 but smaller than Kobayashi et al. (2011) (Tab. 2). The difference can be attributed to  
199 that Kobayashi (2011) adopted double fault to model. In terms of the magnitude, the  
200 result in this study was greater than the others and the CMT mechanism solution result  
201 was the smallest.

202 The fitting and residual interferograms are shown in Fig. 3. From the Fig. 3(a)

203 and (c), the simple uniform slip model obtains a well global fitting with the  
204 observation, but in Iwaki region, there was a 1.5 residual fringe on both sides of the  
205 fault line in Fig. 3(b), mainly because the epicenter position have a sharply  
206 deformation gradient and low coherence, the uniform model were not enough to fit the  
207 deformation; in Kita-Ibarake region, residual was smaller.

#### 208 *4.2 Distributed-Slip Model*

209 To make the model more reliable and better fit the observations, a distributed-slip  
210 model was used to derive more detailed slip distribution. For the Iwaki earthquake, we  
211 extended the Itozawa and Yunotake fault plane to a 22 km length, 30 km width and 24  
212 km length, 30 km width, respectively. Each fault was divided into small patches of 1  
213 km $\times$ 1 km. For the Kita-Ibarake earthquake, the fault plane extended a plane with 8 km  
214 length and 24 km width, and divided into small patches of 0.5 km  $\times$ 0.5 km (because of  
215 only one small fault used in this earthquake, a smaller patch of 0.5 km  $\times$ 0.5 km was  
216 used). In the distributed-slip model, we only needed to solve the slip magnitude and  
217 rake angle on each patch, and the other geometrical parameters fixed by uniform-slip  
218 model, so the slip on fault plane had a linear relationship with the surface deformation.  
219 The best fitting values of strike-slip and dip-slip motion for each patch were solved in  
220 a least-square framework.

221 The inverted slip-distribution was shown in Fig. 4. For the Iwaki earthquake, the  
222 slip of Itozawa and Yunotake fault (Fig. 4(a) and (b)) were mainly concentrated in 0-3  
223 km depth, the maximum slip of Yunotake fault is 2.5 m, smaller than 4.0 m of Itozawa  
224 fault. For the Kita-Ibarake earthquake, fault slip (Fig. 4(c)) is mainly concentrated in

225 2-12 km depth; the maximum slip is 1.5 m. In order to estimate the precision of  
226 slip-distribution on the fault plane, we used the original observation data to create 100  
227 data group with random disturbance error, and calculate the corresponding spatial  
228 slip-distribution results to estimate the precision of the model. From Fig. 4(d-f), it  
229 shows that the maximum model error are 0.3 m, 0.2 m and 0.3 m, respectively, which  
230 indicate that the slip distribution were reliable.

231 The fitting interferogram and residual of the distributed-slip model were shown  
232 in Fig. 5. The inversion results fit well with the observation and the residual errors  
233 were very small (Fig. 5). Residual distribution is shown to have strong randomness,  
234 mainly due to atmosphere delay, DEM error etc.

235 Comparing Fig. 3 with Fig. 5, the distributed-slip inversion expanded the length  
236 and width of fault plane. The faults were divided into small size, and the slip and rake  
237 on each small patch is determined, which could get a more detailed of fault, but the  
238 uniform slip model taken the slip distribution and rake angle on the whole fault surface  
239 as one uniform value. Thus, the results in Fig. 5 were better than the result in Fig. 3.  
240 The residual interferograms in Fig. 3 and Fig. 5 directly reflected the goodness of  
241 fitting, indicating that the distributed-slip model can be more reasonable with the  
242 aftershock deformation field.

## 243 **5. Coulomb Stress Change**

244 Coulomb Failure Criterion is the core of Coulomb stress triggering hypothesis,  
245 and the Coulomb stress change could be defined as  $\Delta CFF = \Delta \tau + \mu \Delta \sigma$  (Toda et al.,  
246 2011), where  $\tau$  is the shear stress on the fault (positive in the inferred direction of

247 slip),  $\sigma$  is the normal stress (positive for fault unclamping), and  $\mu$  is the apparent  
248 friction coefficient. The general hypothesis of Coulomb stress triggering theory is: the  
249 positive  $\Delta CFF$  is promoted failure, while the negative is inhibited.

250 The seismogenic fault plane of the Mw 9.0 Tohoku-Oki event provided by Xu et  
251 al. (2012) was used to calculate the Coulomb stress change on different receive faults.  
252 We adopted the PSGRN/PSCMP software package (Wang et al., 2006), assumed the  
253 frictional coefficient of 0.4 (e. g., Toda et al., 2011), to calculate the Coulomb stress  
254 change in a multi-layers crust model using the parameters from CRUST 2.0 (Mooney  
255 et al., 1998).

#### 256 *5.1 Coseismic Coulomb Stress Changed on Parallelized Mainshock Fault*

257 When the fault parameters of Mw 9.0 Tohoku-Oki event were selected as the  
258 receiver fault, the coseismic Coulomb stress change is shown in Fig. 6(a) with  
259 aftershocks lower than 20 km plotted. It was shown that there were fewer aftershocks  
260 located in the positive Coulomb stress change region and the inland aftershocks  
261 sequence including the testing region have a negative Coulomb stress change. Use the  
262 receiver fault model provided by Toda (2001c), the Coulomb stress change on the  
263 mainshock fault can be calculated as shown in Fig. 6(b). Comparing the results of Fig.  
264 6(a) with Fig. 6(b), it was found that the receiver fault model provided by Toda (2011)  
265 could fit the aftershocks distribution much better. Because the different aftershocks  
266 have a different source mechanism, the above calculation based on space distribution  
267 of aftershocks could not provide an accurate Coulomb stress change for each  
268 aftershock. If there was a source mechanism for one aftershock, more accurate

269 Coulomb stress change on it can be obtained.

## 270 *5.2 Coulomb Stress Change on the Aftershock Faults*

271 After the slip distribution inverted, we computed the Coulomb stress change on  
272 each slip patch (as shown in Fig. 7). For the Iwaki earthquake, the Coulomb stress  
273 changes were 0.64~0.97 MPa (Fig. 7(a)) and 0.04~0.2 MPa (Fig. 7(b)) on the Itozawa  
274 fault and Yunotake fault, respectively. The value of the Coulomb stress change on the  
275 Itozawa fault with 0.97 MPa was much larger than that on the Yunotake fault with 0.2  
276 MPa, suggesting that the static Coulomb stress imparted by the Mw 9.0 Tohoku-Oki  
277 event mainly triggered the aftershock on Itozawa fault, and then triggered the event on  
278 Yunotake fault. For the Kita-Ibarake earthquake, the Coulomb stress change was  
279 0.26~0.65 MPa (Fig. 7(c)) which was consistent with the result of 0.68 MPa in  
280 Kobayashi et al. (2011). In addition, the Coulomb stress change showed a stratified  
281 phenomenon (Fig. 7), which mainly due to the Green function calculation using a  
282 multi-layer crust model. Our results indicate that the Mw 9.0 Tohoku-Oki event  
283 promoted the aftershocks occurrence, which is consistent with result of Toda et al.  
284 (2011b).

## 285 **6. Discussion and Conclusion**

286 The majority of aftershocks following the Tohoku-Oki earthquake are located  
287 near the plate interface in the sea, and moderate to large aftershocks at a deeper depth  
288 may not cause sufficiently strong ground motions to pose a hazard. However, any  
289 shallow aftershocks in the upper crust may represent a significant seismic hazard  
290 because of small source-to-site distances and relatively strong ground motions in

291 frequency ranges of concern to engineered structures (Ryder et al., 2011). The InSAR  
292 data presented in this paper clearly show that the surface deformation of two large  
293 aftershocks were shallow normal fault crustal events.

294 For the Iwaki earthquake, the maximum surface displacement was 2.1 m in LOS  
295 direction which is consistent with the 2 m from field survey by Otsubo et al. (2012).  
296 The strike angle of the Itozawa and Yunotake faults were  $159.4^\circ$  and  $121.5^\circ$  as in the  
297 fig.2 (c). Compared our results with the historical field surveys, the location of  
298 Yunotake fault trace was consistent well and the location of Itozawa fault have a litter  
299 up left shift. Integrating with the pattern of interferogram, the fault trace extracted  
300 from azimuth offsets could be more reliable. For the Kita-Ibarake earthquake, the  
301 maximum surface deformation was 0.44 m, which was close to the 0.4 m in Kobayashi  
302 (2011).

303 Interferograms and seismology results show that the Iwaki earthquake (Fig. 1(b))  
304 and Kita-Ibarake earthquake (Fig. 1(d)) both was shallow normal earthquake. With the  
305 InSAR observations and azimuth offsets to constraint the model, we inverted the  
306 source parameter for the two faults of Iwaki earthquake. The source parameters as  
307 fellows:, the dip angle were  $56^\circ$  and  $48.7^\circ$ , the rake angle were  $-84^\circ$  and  $-73.5^\circ$  for the  
308 two faults, and the magnitude of the Iwaki earthquake is Mw 6.75 which larger than  
309 the Mw 6.6 from CMT. For the Kita-Ibarake earthquake, the dip angle was  $32.8^\circ$ , the  
310 rake angle was  $-103.2^\circ$ , and the magnitude was Mw 6.17 which larger than the Mw 5.8  
311 from CMT, the reason of this different maybe comes from the different data source.  
312 The slip distribution inversion (Fig. 5) indicates that in Iwaki region the deformation is

313 caused by the dislocation of Itozawa and Yunotake fault reached the surface and had a  
314 shallow depth, so it caused a huge surface rupture, consistent with field results; in  
315 Kita-Ibarake region the minimum depth of seismogenic fault is located under the  
316 surface ~2 km, so the surface observation was small, and this type of earthquakes  
317 would cause a slightly hazard.

318       The calculated Coulomb stress changes show that Mw 9.0 magnitude earthquake  
319 promoted the occurrence of the two Events. Many studies of Coulomb stress change  
320 triggering (e. g., Harris, 1998; Stein, 1999; Freed, 2005) find that the static Coulomb  
321 stress change plays an important role in the aftershock on surrounding faults (Toda et  
322 al., 2011). The optimal coulomb stress calculating model (Xu et al., 2009) shows that  
323 the impact factor for Coulomb stress value main includes stress tensor, receiver fault  
324 geometry, pore pressure model and friction coefficient. After the Mw 9.0 Tohoku-Oki  
325 event, the seismicity changes sharply in the whole inland in Japan. In the target region  
326 (Iwaki and Kita-Ibarake), the seismic activity changed from silent before Mw 9.0  
327 event to active after the event. Using onshore GPS observations from 298 stations in  
328 the 2 weeks following the Tohoku earthquake, Evans et al. (2012) suggested that the  
329 afterslip is located almost exclusively down-dip of the coseismic rupture with a  
330 transition between 40 and 50 km depth, indicating the afterslip could not cause the  
331 aftershocks triggering in the targeted region in this study.

332       By using the earthquake catalog data from JMA (2004), some people (Okada et  
333 al., 2011; Toda et al., 2011; Yoshida et al., 2012; Imanishi et al 2012) have research the  
334 stress change in the aftershock region after the Tohoku-Oki earthquake, and they

335 inferred that stress changes caused by Mw 9.0 Tohoku-Oki event have triggered the  
336 normal-faulting earthquake sequence at the Ibaraki-Fukushima prefectural border  
337 which disagree with the inference of Kato et al. (2011) who argued that a reversal of  
338 stress state occurred as a result of the Tohoku-Oki earthquake. However, the seismic  
339 wave and geological data are less practical to obtain accurate fault geometry and slip  
340 distribution of aftershocks. When those imprecise aftershock faults model were used  
341 as the receiver fault to study whether the aftershock is triggered by the mainshock, the  
342 inference of Coulomb stress triggering may be questionable. So the detailed receiver  
343 fault parameters should be taken seriously. In this paper, the Coulomb stress changes  
344 calculated based on detailed aftershock source in the target region and the maximum  
345 value is nearly 1 MPa. Our results indicate the Tohoku-Oki Mw 9.0 earthquake played  
346 an important role to promote the aftershock triggering and agreed with the arguments  
347 of Imanishi et al (2012). Except the stress changes study, Tong et al (2012) use the P  
348 and S wave data achieve the high-resolution tomographic images for the 2011 Iwaki  
349 earthquake (Mj 7.0) and Fukushima nuclear power plant area. Their results also  
350 suggested that the Iwaki earthquake was triggered by the ascending fluids from the  
351 Pacific slab dehydration and the stress variation induced by the Tohoku-Oki event and  
352 supported our results.

353

#### 354 **Acknowledgment**

355 This work is co-supported by the State Key Development Program for Basic  
356 Research of China (No. 2013CB733304), the National Natural Science Foundation of

357 China (Nos. 41074007, 41021061 and 41204010), the Doctoral Fund of Ministry of  
358 Education of China (Nos. 20110141130010, 20090141110055), and the Fundamental  
359 Research Funds for the Central Universities (Nos. 114035, 201121402020007). The  
360 ALOS PALSAR data are provided by JAXA through Geohazard Supersites. All  
361 figures are plotted using Generic Mapping Tools (GMT) version 4.5.1.

362

### 363 **References**

- 364 Active Fault and Earthquake Research Center, 2011. Active fault database of Japan.  
365 [http://riodb02.ibase.aist.go.jp/activefault/index\\_e.html?search\\_no=j008&version](http://riodb02.ibase.aist.go.jp/activefault/index_e.html?search_no=j008&version)  
366 [\\_no=1&search\\_mode=020](http://riodb02.ibase.aist.go.jp/activefault/index_e.html?search_no=j008&version_no=1&search_mode=020)
- 367 Chen, C.W. and Zebker, H.A., 2001. Two-dimensional phase unwrapping with use of  
368 statistical models for cost functions in nonlinear optimization. *Journal of the*  
369 *Optical Society of America*, 18, 338–351.
- 370 Clarke, P.J., Paradissis, D., Briole, P., England, P.C., Parsons, B.E., Billiris, H., Veis,  
371 G., and Ruegg, J.C., 1997. Geodetic investigation of the 13 May 1995  
372 Kozani-Grevena (Greece) Earthquake. *Geophysical Research Letters.*, 24(6),  
373 707-710, doi:10.1029/97GL00430.
- 374 Evans, E.L., and Meade, B.J., 2012. Geodetic imaging of coseismic slip and  
375 postseismic afterslip: Sparsity promoting methods applied to the great Tohoku  
376 earthquake. *Geophysical Research Letters.*, 39, L11314,  
377 doi:10.1029/2012GL051990.
- 378 Farr, M., Rosen, A., Caro, E., 2007. The Shuttle Radar Topography Mission. *Reviews*

379 of Geophysics, 45, RG2004, doi:10.1029/2005RG000183

380 Feng, G.X., Ding, X. L., Li, Z.W., Mi, J., Zhang, L., and Omura, M., 2001. Calibration  
381 of InSAR-derived coseismic deformation map associated with the 2011 Mw 9.0  
382 Tohoku-Oki earthquake. *IEEE Geoscience and Remote Sensing letters.*,  
383 9(2):302-306.

384 Freed, A. M., 2005. Earthquake triggering by static, dynamic and postseismic stress  
385 transfer. *Annual Review of Earth and Planetary Sciences.*, 33:335-67,  
386 doi:10.1029/2006GL029155

387 Fujii, Y., Satake, K., Sakai, S., Shinohara, M., and Kanazawa, T., 2011. Tsunami  
388 source of the 2011 off the Pacific coast of Tohoku earthquake. *Earth Planets and*  
389 *Space*, 63, 815–820, doi:10.5047/eps.2011.06.010.

390 Goldstein, R.M., and Werner, C.L., 1998. Radar interferometry filtering for  
391 geophysical application. *Geophysical Research Letters.*, 25(21):4035-4038

392 Harris, R.A., 1998. Introduction to special section: stress triggers, stress shadows, and  
393 implications for seismic hazard. *Journal of Geophysical Research.*, 103,  
394 24347-34358

395 Hirose, F., Miyaoka, K., Hayashimoto, N., Yamazaki, T., and Nakamura, M., 2011.  
396 Outline of the 2011 off the Pacific coast of Tohoku earthquake (Mw  
397 9.0)-Seismicity: Foreshocks, mainshock, aftershocks, and induced activity. *Earth*  
398 *Planets and Space*, 63, 513–518, doi:10.5047/eps.2011.05.019.

399 Imanishi, K., Ando, R., and Kuwahara, Y., 2012. Unusual shallow normal-faulting  
400 earthquake sequence in compressional northeast Japan activated after the 2011 off

401 the Pacific coast of Tohoku earthquake. *Geophysical Research Letters.*, 39,  
402 L09306, doi:10.1029/2012GL051491.

403 Japan Meteorological Agency (JMA), 2004. *The Seismological and Volcanological*  
404 *Bulletin of Japan for January 2004*, Tokyo.

405 Kato, A., Sakai, S., and Obara, K., 2011. A normal-faulting seismic sequence  
406 triggered by the 2011 off the Pacific coast of Tohoku earthquake: Wholesale  
407 stress regime changes in the upper plate. *Earth Planets and Space*, 63, 745–748,  
408 doi:10.5047/eps.2011.06.014.

409 Kobayashi, T., Tobita, M., Nishimura, T., Suzuki, A., Noguchi, Y., and Yamanaka, M.,  
410 2011. Crustal deformation map for the 2011 off the Pacific coast of Tohoku  
411 Earthquake, detected by InSAR analysis combined with GEONET data. *Earth*  
412 *Planets and Space*, 63, 621–625, 2011

413 Kubo, A., Fukuyama, E., Kawai, H., and Nonomura, K., 2002. NIED seismic moment  
414 tensor catalogue for regional earthquakes around Japan: Quality test and  
415 application. *Tectonophysics*, 356, 23–48, doi:10.1016/S0040-1951(02)00375-X.

416 Loveless, J.P., and Meade, B.J., 2011. Spatial correlation of interseismic coupling and  
417 coseismic rupture extent of the 2011 MW = 9.0 Tohoku-oki earthquake.  
418 *Geophysical Research Letters.*, 38, L17306, doi:10.1029/2011GL048561.

419 Massonnet, D., Rossi, M., Carmona, C., Adragna, F., Peltzer, G., Feigl, K., Rabaute,  
420 T., 1993. The displacement field of the Landers earthquake mapped by radar  
421 interferometry. *Nature*, 364: 138-142

422 Mooney, W.D., Laske, G., Masters, T.G., 1998. CRUST 5. 1: A global crustal model

423 at  $5^{\circ} \times 5^{\circ}$ . Journal of Geophysical Research, 103: 727–747

424 Okada, Y., 1985. Surface deformation due to shear and tensile faults in a half-space.  
425 Bulletin of the Seismological Society of America., 75 (4), 1135-1154.

426 Okada, T., Yoshida, K., Ueki, S., Nakajima, J., Uchida, N., Matsuzawa, T., Umino, N.,  
427 Hasegawa, A., 2011. Shallow inland earthquake in NE Japan possibly triggered  
428 by the 2011 off the Pacific coast of Tohoku Earthquake. Earth Planets and Space,  
429 63: 749-754

430 Otsubo, M., Shigematsu, N., Takahashi, M., Azuma, T., Imanishi, K., and Ando, R.,  
431 2012. Slickenlines on fault scarps caused by an earthquake in Iwaki-city  
432 (Fukushima Prefecture, Japan) on 11th of April, 2011. Journal of the Geological  
433 Society Japan., 118, 3-4.

434 Ryder, I., Rietbrock, A., Kelson, K., Bürgmann, R., Floyd, M., Socquet, A., Vigny, C.,  
435 and Carrizo, D., 2011. Large extensional aftershocks in the continental forearc  
436 triggered by the 2010 Maule earthquake, Chile. Geophysical Journal International.  
437 188, 879–890 doi: 10.1111/j.1365-246X.2011.05321.x

438 Simons, M., Fialko, Y., and Rivera, L., 2002. Coseismic deformation from the 1999  
439 Mw 7.1 Hector Mine, California, earthquake as inferred from InSAR and GPS  
440 observations. Bulletin of the Seismological Society of America.,  
441 92(4):1390-1402

442 Stein, R. S., 1999. The role of stress transfer in earthquake occurrence. Nature, 402,  
443 606-609

444 Toda, S., Lin, J., Stein, R.S., 2011. Using the 2011 Mw 9.0 off the Pacific coast of

445 Tohoku Earthquake to test the Coulomb stress triggering hypothesis and to  
446 calculate faults brought closer to failure. *Earth Planets and Space*, 63:725-730

447 Toda, S., 2011, <http://www.usgsprojects.org/TohokuQuake2011/>

448 Tong, P., Zhao, D. & Yang, D., 2012. Tomography of the 2011 Iwaki earthquake (M7.0)  
449 and Fukushima nuclear power plant area. *Solid Earth* 3, 43-51,  
450 doi:10.5194/se-3-43-2012

451 Townend, J., and Zoback, M.D., 2006. Stress, strain, and mountain building in central  
452 Japan, *Journal of Geophysical Research.*, 111, B03411,  
453 doi:10.1029/2005JB003759.

454 Wang, R., Lorenzo-Martín, F., Roth, F., 2006. PSGRN/PSCMP - A new code for  
455 calculating co- and post-seismic deformation, geoid and gravity changes based on  
456 the viscoelastic-gravitational dislocation theory. *Computational Geosciences.*, 32:  
457 527–541

458 Werner. C., Wegmüller, U., Strozzi, T., Wiesmann, A., 2000. GAMMA SAR and  
459 interferometry processing software. ERS ENVISAT Symposium, Gothenburg,  
460 Sweden, 16-20.

461 Wright, T.J., Parsons, B.E., Jackson, J.A., Haynes, M., Fielding, E.J., England, P.C.,  
462 Clarke, P.J., 1999. Source parameters of the 1 October 1995 Dinar (Turkey)  
463 earthquake from SAR interferometry and seismic body wave modelling. *Earth  
464 and Planetary Science Letters*. 172, 23-37.

465 Xu, C.J., Wang, J.J., Li, Z.H., Drummond, J., 2009. Applying the Coulomb failure  
466 function with an optimally oriented plane to the 2008 Mw 7.9 Wenchuan

467 earthquake triggering. *Tectonophys.*, 2009, doi:10.1016/j.tecto.2009.09.019.

468 Xu, C.J., He, P., Wen, Y.M., Zhang, L., 2012. Coseismic Deformation and Slip  
469 Distribution for the 2011 Tohoku-Oki Mw 9.0 Earthquake: Constrained by GPS  
470 and InSAR. *Geomatics and Information Science of Wuhan University* (in press)

471 Yoshida, K., Hasegawa, A., Okada, T., Inuma, T., Ito, Y. and Asano, Y., 2012. Stress  
472 before and after the 2011 great Tohoku-oki earthquake and induced earthquakes in  
473 inland regions of eastern Japan. *Geophysical Research Letters.*, 39, L03302,  
474 doi:10.1029/2011GL049729.

475 Zoback, M. L., 1992. First- and second-order patterns of stress in the lithosphere: The  
476 world stress map project. *Journal of Geophysical Research.*, 97, 11,703–11,728,  
477 doi:10.1029/92JB00132.

478 **Tab captions**

479 Tab. 1 Interferometry pairs used in this study

480 Tab. 2 The source parameters from our study and CMT solution

481 Tab. 3 multilayered crustal model parameters

482

483 **Figure captions**

484 Fig. 1 Inland earthquakes occurred during the PALSAR data acquisition time in the  
485 testing region. a) spatial position of PALSAR data overlap region; b) the spatial  
486 distribution of earthquakes occurred during the time span from 2011/3/3 to 2011/4/18  
487 in the Track 403 overlap region; c) the focal depth statistics for the events in (b); d) the  
488 spatial distribution of earthquakes occurred during the time span from 2011/2/2 to  
489 2011/3/20 in the Track 404 overlap region; e) the focal depth statistics for the events in  
490 (d).

491 Fig. 2 Differential Interferogram, Calibration Interferogram and azimuth offset. (a), (b)  
492 and (c) for T403; (d), (e), (f) for T404. The yellow square points in the Interferogram  
493 are the GPS stations.

494 Fig. 3 The fitted interferograms and residuals for the uniform slip model. (a) and (b)  
495 for Track T403, (c) and (d) for Track T404.

496 Fig. 4 Inverted slip distribution and their estimated error. (a) and (d) for Itozawa fault  
497 plane in Iwaki region, (b) and (e) for Yunotake fault plane in Iwaki region, (c) and (f)  
498 for the single fault plane in Kita-Ibarake region.

499 Fig. 5 The fitted interferograms and residuals for the distributed slip model. (a) and (b)

500 for Track T403, (c) and (d) for Track T404.

501 Fig. 6 Static Coulomb stress changes induced by the Mw 9.0 Tohoku-Oki earthquake  
502 and resolved on receiver faults parallel to the main fault (a) and on optimally oriented  
503 planes (Toda, 2011) (b) at depth 20 km. Black dots represent all the aftershock with  
504 magnitudes ranging from 0.1 to 7 during the period from 2011/3/11 to 2011/7/15.

505 Fig. 7 Coulomb stress change on different fault planes. (a) Itozawa fault plane in Iwaki  
506 region, (b)Yunotake fault plane in Iwaki region, (c) the single fault plane in Kita-Ibarake  
507 region.



23 multilayered elastic half-space, which indicates that the maximum slips for the two  
24 earthquakes are 3.28 m and 0.98 m, respectively. The Coulomb stress changes were  
25 calculated for the faults following the 2011 Mw 9.0 Tohoku-Oki earthquake based on  
26 the modeled slip along the fault planes. The resulting Coulomb stress changes indicate  
27 that the stresses on the faults increased by up to 1.1 MPa and 0.7 MPa in the Iwaki and  
28 Kita-Ibarake regions, respectively, suggesting that the Tohoku-Oki earthquake  
29 triggered the two aftershocks, supporting the results of seismic tomography.

30 **Key words:** Tohoku-Oki earthquake, InSAR, slip distribution inversion, Coulomb  
31 stress change, aftershock triggering

## 32 **1. Introduction**

33 The Mw 9.0 Tohoku-Oki earthquake (USGS 38.322°N, 142.369°E) occurred on  
34 March 11, 2011, in the Pacific Ocean east of Japan (Fig. 1(a)), where the Pacific plate  
35 subducts beneath Honshu at a rate of ~9 cm/yr (Imanishi et al., 2012). Due to the  
36 release of long-term accumulated stress, it generated a tsunami that caused significant  
37 damage locally in Sendai. Several estimates of the fault slip distribution have been  
38 published (e.g., Fujii et al., 2011; Loveless and Meade, 2011; Yoshida et al., 2012),  
39 indicating a coseismic slip exceeding 30 m over a wide region.

40 The Tohoku-Oki earthquake has caused large variations in the stress field both  
41 near the source and far from the epicenter, causing a significant increase in seismic  
42 activity in the crust of the overriding plate west of the source area (Okada et al., 2011).  
43 Thousands of aftershocks occurred in the first few months following the Tohoku-Oki  
44 earthquake. Two major aftershocks were the Iwaki earthquake (Mj 7.0), which  
45 occurred in a previous seismic gap on April 11, 2011, and was the strongest on-land  
46 aftershock, and the Kita-Ibarake earthquake (Mj 6.0), which occurred on March 19,  
47 2011 (note: Mj is the quick response magnitude and CMT is the centroid-moment  
48 tensor calculated by the Japan Meteorological Agency (JMA); both are reported by the  
49 NEID (<http://www.fnet.bosai.go.jp/event/search.php?LANG=en>)). We aimed to  
50 answer two main questions regarding these large aftershocks. First, what were the  
51 focal mechanisms of the earthquakes? Other than the CMT solution from the NEID,  
52 there is little published information about the slip distributions. Kobayashi et al. (2012)  
53 used InSAR data to detect the Iwaki earthquake. Second, were the two events

54 triggered by the Tohoku-Oki earthquake? Using earthquake catalog data from the JMA  
55 (2004), the Coulomb stress changes on the fault planes of the Iwaki and Kita-Ibarake  
56 earthquakes have been calculated in some studies (e.g., Okada et al., 2011; Toda et al.,  
57 2011; Imanishi et al., 2012).

58 In this study, we used geodetic data (GPS and InSAR) to constrain the location,  
59 geometry and slip distribution of the two earthquakes. Then, we tested whether these  
60 earthquakes were caused by the Tohoku-Oki earthquake.

## 61 **2. Geological background**

62 As located at a plate boundary, earthquakes occur frequently in Japan. After The  
63 Mw 9.0 Tohoku-Oki earthquake there were several  $M \geq 6$  earthquakes occurred inland  
64 and off Japan's western coast in the Japan Sea (Hirose et al., 2011). These aftershocks  
65 included an Mj 7.0 earthquake on April 11, 2011, and nine moderately sized  
66 earthquakes ( $M_j \geq 5.0$ ) after April 18, 2011. Based on seismic waveforms, the focal  
67 mechanism of the largest aftershock in the study region from the JMA indicates that  
68 these earthquakes were normal faulting events. The aftershock depths (Fig. 1(c) and  
69 (e)) indicate that most aftershocks occurred at depths shallower than 20 km. However,  
70 the area of the Iwaki and Kita-Ibarake earthquakes, in Fukushima prefecture,  
71 northeastern Japan, had lower background seismicity before the 2011 Tohoku-Oki  
72 earthquake (Imanishi et al., 2012).

73 The two aftershocks focused on in this study occurred in the western Iwaki city of  
74 Abukuma-sanchi. Metamorphic rocks and Cretaceous strata, granite and epidiorite are  
75 distributed throughout this area, as are forearc deposits with a Tertiary unconformity

76 (Kubo et al. 2007). Previous field investigations indicate that there are active  
77 strike-slip and normal faults, including the Itozawa Fault and the Yunotake Fault,  
78 which have orientations of N10°W strike, 70°W dip and N60°W strike, 60°S dip,  
79 respectively (Active Fault and Earthquake Research Center, 2011). The Mj 7.0 Iwaki  
80 earthquake produced a 14-km-long westward normal-slip rupture on the Itozawa Fault  
81 and a 16-km-long southward normal-slip rupture on the Yunotake Fault. The  
82 northwestern end of the rupture on the Yunotake Fault is ~2.5 km from the  
83 northwestern end of the Itozawa Fault (Mizoguchi et al., 2012). Both faults have  
84 normal fault scarps with offsets of up to 2 m (e.g., Otsubo et al., 2012). The Yunotake  
85 Fault coincides with a ~200-m-high scarp, which is the result of geologically recent  
86 normal faulting or erosion that bounds the Neogene and pre-Neogene rocks (Kubo et  
87 al., 2007). The Itozawa Fault developed within the Gosaisho metamorphic rocks and is  
88 composed of three strands (Mizoguchi et al., 2012). Although both the Yunotake and  
89 Itozawa faults have been recognized as active (Nakata and Imaizumi, 2002), their  
90 paleoseismic histories are poorly understood. This normal faulting is inconsistent with  
91 the present-day regional stress field in northeastern Japan, which is characterized by a  
92 reverse-faulting regime with E-W compression (e.g., Zoback, 1992; Kubo et al., 2002;  
93 Townend and Zoback, 2006). In the northern Kita-Ibarake region, the seismicity  
94 changed drastically from a quiescent stage to an active stage, with no previously  
95 identified active faults.

### 96 **3. InSAR Surface Displacements and Fault Characteristics**

#### 97 *3.1 InSAR analysis*

98           Phased Array type L-band Synthetic Aperture Radar (PALSAR) images from the  
99   Advanced Land Observing Satellite (ALOS) were selected to derive the crustal  
100   deformation field for the study area of the Iwaki and Kita-Ibarake regions (Fig. 1(a)).  
101   The distributions of aftershocks in the study region are shown in Figs. 1(b) and (d) for  
102   the PALSAR data acquisition period. The origin times of  $M_j > 5.0$  earthquakes are  
103   shown in Figs. 1(b) and (d), and there were no large earthquakes ( $M_j > 5.0$ ) prior to the  
104   Mw 9.0 Tohoku-Oki earthquake. The depths of the earthquakes were concentrated at  
105   depths of 2–16 km, as shown in Figs. 1(c) and (e).

106           Two interferometric pairs were constructed from the PALSAR data (Tab. 1). The  
107   SAR data were processed from raw products with the conventional two-pass  
108   differential interferometry approach (Massonnet et al., 1993) using the GAMMA  
109   software package (Werner et al., 2000). To ensure a high signal-to-noise ratio (SNR), a  
110   3:8 multi-look ratio was applied to the PALSAR data in the azimuth and range  
111   directions during processing. The 3-arc second SRTM DEM (Farr et al., 2007) was  
112   used to remove the phase component due to topography. To further reduce the phase  
113   noise and to improve the interferogram quality, a power spectrum filter (Goldstein et  
114   al., 1998) was applied to filter the interferograms. The minimum-cost flow algorithm  
115   (Chen and Zebker, 2001) was adopted to unwrap the differential interferograms. The  
116   geocoded interferograms are shown in Figs. 2(a) and (d) (one fringe represents 11.8  
117   cm of deformation in all interferograms shown in this paper). In the Figs. 2(a) and (d)  
118   show very dense fringes, with nearly 20 fringes in Fig. 2(a) and nearly 10 fringes in  
119   Fig. 2(d).

120 The contributions to the interferograms (Figs. 2(a) and (d)) include the coseismic  
 121 deformation of the Tohoku-Oki earthquake, deformation due to large aftershocks,  
 122 orbital errors, atmosphere delays and a topographic error phase. The atmospheric  
 123 delays and topographic error phase are considered relatively small compared with the  
 124 deformation (e.g., Feng et al., 2011) and are not considered further in this study. The  
 125 phase contributions can be expressed as follows:

$$126 \quad d_{insar} = d_{Mw9.0} + d_{orbit} + d_{deformation} + d_{error}, \quad (1)$$

127 where  $d_{orbit}$  is the orbit error and can be removed by the polynomial method (e.g.,  
 128 Hanssen, 2001);  $d_{Mw9.0}$  and  $d_{deformation}$  are the coseismic and aftershock deformation,  
 129 respectively; and  $d_{error}$  is the white noise. We can interpolate the dense GPS  
 130 observations of coseismic deformation to obtain the InSAR-based coseismic  
 131 deformation  $d_{Mw9.0}$ . Thus, formula (1) can be rewritten as follows:

$$132 \quad d_{deformation} = d_{insar} - d_{orbit} - d_{Mw9.0} - d_{noise} . \quad (2)$$

133 After removing  $d_{Mw9.0}$ , the corrected interferograms are shown in Figs. 2 (b) and (e).  
 134 The corrected interferogram in Fig. 2(b) indicates that the maximum displacement was  
 135 2.1 m in the line-of-sight (LOS) range. Our results are consistent with the field surveys,  
 136 which show that the Iwaki earthquake caused several normal faulting surface ruptures  
 137 and up to 2 m of deformation (Otsubo et al., 2012). The corrected interferogram in Fig.  
 138 2(e) shows up to 0.44 m of deformation in the LOS range, which is in good agreement  
 139 with the ~0.4 m indicated by a previous InSAR study (Kobayashi et al., 2011).

### 140 *3.2 Azimuth offsets*

141 In addition to phase information, SAR images also contain amplitude information,

142 which is a function of the intensity of image backscattering. The deviation between the  
143 surface deformation and the satellite orbit, as well as the amplitude differences of the  
144 SAR image before and after the earthquake, suggests that each pixel has an offset in  
145 the azimuth and range direction. For earthquakes in remote regions and for large  
146 numbers of aftershocks, it is often difficult to obtain accurate field observations of the  
147 surface rupture (Simons et al., 2002), but SAR-based azimuth offsets can be easily  
148 used to determine the surface trace of a seismogenic fault. In this study, the azimuth  
149 offsets were calculated from two accurate registration images along the orbit direction  
150 deviation. The accuracy of the azimuth offset is less than that of the phase observation,  
151 and the mean of the azimuth offset is less sensitive to the surface deformation than to  
152 the coherence coefficient. Therefore, high-quality azimuth offsets can be obtained  
153 even in an incoherent region (such as the high deformation gradient near a fault).  
154 Normally, the azimuth offsets can provide an accurate fault trace. The azimuth offsets  
155 of the interference pairs T403 and T404 are shown in Figs. 2(c) and (f).

156 In Fig. 2(c), the solid red lines show the Itozawa and Yunotake faults from field  
157 observations (Active Fault and Earthquake Research Center, 2011), and the solid green  
158 line shows the corresponding fault traces extracted by the azimuth offsets. A  
159 comparison of the fault traces from the geological field investigations and using the  
160 azimuth offsets shows that the Yunotake Fault trace is well constrained. The absolute  
161 location of the Itozawa Fault trace is uncertain, but its orientation and length are well  
162 constrained. The fault trace extracted using azimuth offsets could be more accurate if  
163 it were integrated with the interferogram. The strike direction and the location of the

164 Itozawa and Yunotake faults can be determined by the azimuth offset method (Tab. 2).

165 As shown in Fig. 2(f), the fault trace cannot be identified using azimuth offsets  
166 for the T404 interferogram pair, and no corresponding seismogenic fault was detected  
167 from field surveys (JMA, 2004). We conclude that the seismogenic fault associated  
168 with this event is a blind fault.

#### 169 **4. Modeling of Fault Parameters**

170 We inverted the InSAR observations (Figs. 2(b) and (e)) for the geometry and slip  
171 distribution of the seismogenic faults responsible for the aftershocks. The  
172 interferograms were down-sampled to decrease the size of the dataset and accelerate  
173 the inversion.

##### 174 *4.1 Uniform-Slip Model*

175 To determine the source mechanism for the aftershocks, InSAR datasets were  
176 modeled with uniform slip on a rectangular dislocation in an elastic half-space (Okada,  
177 1985). Nine fault parameters (longitude, latitude, length, minimum depth, maximum  
178 depth, strike, dip, slip and rake) were determined in this inversion procedure, which  
179 minimizes the misfit between the observations and predicted values using a non-linear,  
180 downhill simplex algorithm with multiple Monte Carlo iterations to avoid local  
181 minima (Clarke et al., 1997; Wright et al., 1999). Although the InSAR data were  
182 processed with precise orbit information, the interferogram still contained residual  
183 orbit errors, so a linear function was applied to the inverted model to estimate the  
184 residual orbit error. The inverted model can be written as follows:

$$185 \quad d_{InSAR} = Gm + \varepsilon, \quad (3)$$

186 where  $d_{InSAR}$  is the InSAR observations,  $G$  is the design matrix,  $m$  is the  
187 parameter dataset, including fault parameters and orbit parameters, and  $\varepsilon$  is the  
188 observation noise. The ultimate goal of the inversion is to optimally fit the model to  
189 the observed data to minimize the objective function.

190 For the Iwaki earthquake, a two-fault model was used to invert the source  
191 mechanism. The fault locations and strike angles were fixed based on the azimuth  
192 offsets and the geological survey. The inverted fault parameters are given in Tab. 2.  
193 The Itozawa and Yunotake faults experienced normal faulting with rake angles of  $88.4^\circ$   
194 and  $73.5^\circ$ , respectively. The motion along these faults was mainly dip-slip with a small  
195 amount of strike-slip motion, and the total seismic moment was  $1.673 \times 10^{19}$  N m (Mw  
196 6.75). There were several Mw 5.5-6.6 earthquakes that occurred during the SAR data  
197 acquisition period; the epicenters of these earthquakes are shown in Fig. 1. Although it  
198 is difficult to identify the deformation caused by individual earthquakes using the  
199 available geodetic data, the deformation indicated by the interferogram in Fig. 2(a) can  
200 be used for an initial estimate. In addition, small earthquakes (Mw<6.0) would not  
201 have produced large surface ruptures, so the deformation in interferogram T403 was  
202 mainly caused by the Mj 7.0 Iwaki earthquake. The dip and rake angles are similar to  
203 the CMT solution but are smaller than that of Kobayashi et al. (2012) (Tab. 2). The  
204 seismic moment is slightly larger than for the CMT solution but smaller than that of  
205 Kobayashi et al. (2012) (Tab. 2).

206 For the Kita-Ibarake earthquake, a one-fault model was used to invert for its  
207 source mechanism. The strike was fixed at  $155^\circ$  based on the interferogram, and the

208 inverted fault parameters are shown in Tab. 2. The rake is  $103.2^\circ$ , which indicates  
209 nearly normal motion. The slip had a significant dip-slip component with a small  
210 amount of strike-slip motion. The minimum depth at which slip occurred was 1.96 km,  
211 indicating that this is a blind fault that caused a small amount of surface deformation,  
212 with no obvious azimuth offsets in Fig. 2(f). The seismic moment was  $2.28 \times 10^{18}$  N m  
213 (Mw 6.17). The dip angle was similar the CMT solution but smaller than that of  
214 Kobayashi et al. (2011) (Tab. 2). This difference can be attributed to the use of two  
215 faults in the Kobayashi et al. (2011) model. The magnitude determined in this study is  
216 larger than that determined by Kobayashi et al. (2011) and that of the CMT, which is  
217 the smallest of the three.

218 The modeled and residual interferograms are shown in Fig. 3. The uniform-slip  
219 model (Figs. 3(a) and (c)) provides a good fit to the observations overall, but there are  
220 1.5 residual fringes on both sides of the fault in the Iwaki region (Fig. 3(b)). This  
221 misfit is mainly due to the sharp deformation gradient and low coherence near the  
222 epicenter. In the Kita-Ibarake region, the residuals are smaller.

#### 223 *4.2 Distributed-Slip Model*

224 To make the model more reliable and to improve the fit to the observations, a  
225 distributed-slip model was used to derive a more detailed slip distribution. For the  
226 Iwaki earthquake model, we extended the Itozawa and Yunotake fault planes to  
227 lengths of 22 km and 24 km, respectively, both with widths of 30 km. Each fault was  
228 divided into 1 km $\times$ 1 km patches. For the Kita-Ibarake earthquake, the fault plane was  
229 extended to a length of 8 km and a width of 24 km. Because only one fault was used to

230 model this earthquake, the fault plane was divided into 0.5 km×0.5 km patches. In the  
231 distributed-slip model, we solved for the slip magnitude and rake on each patch, and  
232 the other geometrical parameters were fixed based on the uniform-slip model so that  
233 the fault slip has a linear relationship with the surface deformation. The best-fitting  
234 amounts of strike-slip and dip-slip motion for each patch were solved within a  
235 least-squares framework.

236 The resulting slip distribution is shown in Fig. 4. For the Iwaki earthquake, the  
237 slip along the Itozawa and Yunotake faults (Figs. 4(a) and (b)) was mainly  
238 concentrated at depths of 0-3 km. The maximum slip of the Yunotake Fault was 2.5 m,  
239 less than the 4.0 m slip of the Itozawa Fault. For the Kita-Ibarake earthquake, the slip  
240 (Fig. 4(c)) was mainly concentrated at depths of 2-12 km, with a maximum slip of 1.5  
241 m. To estimate the precision of the slip distributions, we used the original observations  
242 to create 100 datasets with random errors and calculated the corresponding spatial slip  
243 distributions. Figs. 4(d-f) show that the maximum model errors are 0.3 m, 0.2 m and  
244 0.3 m for the Itozawa, Yunotake, and Kita-Ibarake faults, respectively, which indicates  
245 that the slip distributions are reliable.

246 The interferogram produced by the best-fit distributed-slip model and its  
247 residuals are shown in Fig. 5. The model fits the observations well, and the residual  
248 errors are very small (Fig. 5). The residual distribution is very random, which is  
249 mainly a result of factors such as atmospheric delays and DEM errors.

250 Comparing Fig. 3 with Fig. 5 reveals that the distributed-slip inversion extended  
251 the lengths and widths of the fault planes. The faults were divided into smaller cells.

252 Then, the slip and rake for each cell were determined, thus producing a more detailed  
253 model of each fault, while the uniform-slip model assumed a constant slip distribution  
254 and rake for each fault. Thus, the results in Fig. 5 are better than those in Fig. 3. The  
255 residual interferograms in Figs. 3 and 5 directly reflect the goodness-of-fit of each  
256 model, indicating that the distributed-slip model produces a more realistic deformation  
257 field.

## 258 **5. Coulomb Stress Changes**

259 The Coulomb failure criterion is the core of the Coulomb stress triggering  
260 hypothesis. Coulomb stress changes can be defined as  $\Delta CFF = \Delta\tau + \mu\Delta\sigma$  (King et  
261 al., 1994), where  $\tau$  is the shear stress on the fault (positive in the inferred direction  
262 of slip),  $\sigma$  is the normal stress (positive for fault unclamping), and  $\mu$  is the  
263 apparent friction coefficient. The general hypothesis of Coulomb stress triggering is  
264 that a positive  $\Delta CFF$  promotes failure, and a negative value inhibits failure.

265 The seismogenic fault plane of the Tohoku-Oki earthquake from Xu et al. (2012)  
266 was used to calculate the Coulomb stress changes on different receiving faults. We  
267 adopted the PSGRN/PSCMP software package (Wang et al., 2006) and assumed a  
268 frictional coefficient of 0.4 (e.g., Toda et al., 2011) to calculate the Coulomb stress  
269 change in a multi-layered crust model using the parameters from CRUST 2.0 (Mooney  
270 et al., 1998).

### 271 *5.1 Coseismic Coulomb Stress Changes on a Parallelized Mainshock Fault*

272 For a receiving fault with the same parameters as the source fault of the  
273 Tohoku-Oki earthquake, the coseismic Coulomb stress changes were calculated and

274 are shown in Fig. 6(a) with aftershocks within 20 km. There were fewer aftershocks in  
275 the region of positive Coulomb stress changes, and the area of the inland aftershock  
276 sequence, including the study region, had a negative Coulomb stress change. The  
277 Coulomb stress changes on the mainshock fault were calculated (Fig. 6(b)) using the  
278 receiver fault model of Toda (2001). Comparing Fig. 6(a) with Fig. 6(b) reveals that  
279 the receiver fault model provided by Toda (2011) fits the aftershock distribution much  
280 better than the model using the Tohoku-Oki receiver fault. Because different  
281 aftershocks have different source mechanisms, the calculation based on the spatial  
282 distribution of aftershocks does not provide an accurate Coulomb stress change for  
283 each aftershock. If the source mechanism for an aftershock is available, it can be used  
284 to calculate more accurate Coulomb stress changes.

## 285 *5.2 Coulomb Stress Change on the Aftershock Faults*

286 After inverting for the slip distribution, we computed the Coulomb stress change  
287 on each slip patch (Fig. 7). For the Iwaki earthquake, the Coulomb stress changes were  
288 0.64~0.97 MPa (Fig. 7(a)) on the Itozawa Fault and 0.04~0.2 MPa (Fig. 7(b)) on the  
289 Yunotake Fault. The larger Coulomb stress change on the Itozawa Fault suggests that  
290 the static Coulomb stress imparted by the Tohoku-Oki earthquake mainly triggered the  
291 aftershock on the Itozawa Fault and then triggered the slip along the Yunotake Fault.  
292 For the Kita-Ibarake earthquake, the Coulomb stress change was 0.26~0.65 MPa (Fig.  
293 7(c)), which is consistent with the value of 0.68 MPa calculated by Kobayashi et al.  
294 (2011). In addition, the Coulomb stress change showed a stratified phenomenon (Fig.  
295 7), which is mainly due to the Green's function calculation using a multi-layer crustal

296 model. Our results indicate that the Tohoku-Oki earthquake promoted aftershocks,  
297 which is consistent with result of Toda et al. (2011).

## 298 **6. Discussion and Conclusion**

299 The majority of aftershocks following the Tohoku-Oki earthquake are located  
300 near the plate interface offshore. Moderate-to-large aftershocks at greater depths may  
301 not cause ground motion strong enough to pose a hazard. However, shallower  
302 aftershocks in the upper crust may represent a significant seismic hazard due to small  
303 source-to-site distances and relatively strong ground motions within frequency ranges  
304 of concern for engineered structures (Ryder et al., 2011). The InSAR data presented in  
305 this paper clearly show that surface deformation was caused by two large shallow  
306 normal-faulting crustal aftershocks.

307 For the Iwaki earthquake, the maximum surface displacement was 2.1 m in the  
308 LOS direction, which is consistent with the 2 m displacement found by Otsubo et al.  
309 (2012) in a field survey. The strikes of the Itozawa and Yunotake faults are  $159.4^\circ$  and  
310  $121.5^\circ$ , respectively (Fig. 2(c)). Comparing our results with historical field surveys  
311 shows consistent results for the location of the Yunotake Fault trace and a shift in the  
312 location of the Itozawa Fault. Integrating interferogram data could improve the  
313 reliability of the fault traces extracted from azimuth offsets. The Kita-Ibarake  
314 earthquake produced up to 0.44 m of surface deformation, which is similar to the 0.4  
315 m of deformation from the study by Kobayashi et al. (2011).

316 Interferograms and seismology show that the Iwaki earthquake (Fig. 1(b)) and the  
317 Kita-Ibarake earthquake (Fig. 1(d)) were both shallow normal-faulting earthquakes.

318 Using InSAR observations and azimuth offsets to constrain the model, we inverted the  
319 source parameters for the two faults involved in the Iwaki earthquake: one fault has a  
320 dip of  $56^\circ$  and a rake of  $-88.4^\circ$ , and the second has a dip of  $48.9^\circ$  and a rake of  $-73.5^\circ$ .  
321 These orientations differ from those of Kobayashi et al. (2012), who found dips of  
322  $57.4^\circ$  and  $79.7^\circ$  and rakes of  $-102.3^\circ$  and  $-107.3^\circ$ , respectively, for the two faults. Our  
323 inversion indicates that the magnitude of the Iwaki earthquake was Mw 6.75, larger  
324 than the Mw 6.6 of the CMT solution but smaller than that of Kobayashi et al. (2012).  
325 For the Kita-Ibarake earthquake, we found a fault dip of  $32.8^\circ$ , a rake of  $-103.2^\circ$  and a  
326 Mw of 6.17, which is larger than the Mw 5.8 of the CMT solution. This difference  
327 may arise from the different data sources for the two solutions. The result of the slip  
328 distribution inversion (Fig. 5) indicates that the deformation in the Iwaki region was  
329 caused by slip along the Itozawa and Yunotake faults that caused a large surface  
330 rupture, consistent with field results. In the Kita-Ibarake region, the minimum depth of  
331 the seismogenic fault is  $\sim 2$  km, so there is little surface deformation and thus little  
332 seismic hazard for this type of earthquake.

333 The Coulomb stress changes show that the Tohoku-Oki earthquake promoted the  
334 occurrence of the Iwaki and Kita-Ibarake earthquakes. Many studies of Coulomb  
335 stress change triggering (e.g., Harris, 1998; Stein, 1999; Freed, 2005) have found that  
336 static Coulomb stress changes play an important role in causing aftershocks on  
337 neighboring faults following a larger earthquake (Toda et al., 2011). The Coulomb  
338 stress model (Xu et al., 2010) shows that Coulomb stresses are mainly affected by the  
339 stress tensor, the receiver fault geometry, pore pressures and the friction coefficient.

340 After the Tohoku-Oki earthquake, seismicity changed abruptly throughout inland  
341 Japan. In the study region (Iwaki and Kita-Ibarake), seismicity was non-existent  
342 before the Tohoku-Oki earthquake. Using onshore GPS observations from 298 stations  
343 in the 2 weeks following the Tohoku-Oki earthquake, Evans et al. (2012) suggested  
344 that the afterslip was located almost exclusively down-dip of the coseismic rupture,  
345 with a transition between a depth of 40 to 50 km, indicating the afterslip did not trigger  
346 aftershocks in the study region.

347 By using earthquake catalog data from the JMA (2004), some studies (Okada et  
348 al., 2011; Toda et al., 2011; Yoshida et al., 2012; Imanishi et al., 2012) have focused on  
349 the stress changes in the aftershock region after the Tohoku-Oki earthquake. These  
350 studies have found that stress changes caused by the Tohoku-Oki earthquake triggered  
351 the normal-faulting earthquake sequence at the Ibaraki-Fukushima prefectural border.  
352 This finding conflicts with the inference of Kato et al. (2011), who argued that a  
353 reversal of stresses occurred as a result of the Tohoku-Oki earthquake. Seismic and  
354 geological data are less practical for obtaining accurate fault geometries and the slip  
355 distributions for aftershocks. When imprecise aftershock fault models are used to  
356 determine the receiver fault for Coulomb stress modeling, the results regarding  
357 whether an aftershock was triggered by the mainshock may be questionable. Therefore,  
358 detailed receiver fault parameters are necessary.

359 In this study, Coulomb stress changes were calculated based on detailed  
360 aftershock slip models, and stress increases of nearly 1 MPa were found. Our results  
361 indicate that the Tohoku-Oki earthquake played an important role in triggering

362 aftershocks, in agreement with the arguments of Imanishi et al. (2012). Although  
363 Kobayashi et al. (2012) also used InSAR data to invert the fault parameters of the  
364 Iwake and Kito-Ibarake earthquakes, they determined a steeper dip and larger rake  
365 angle than we found. They found negative  $\Delta CFF$  values in the area and inferred  
366 that static stress changes did not play a role in promoting these earthquakes.

367 For the northeast Japan arc, there exhibit strong lateral heterogeneity under the  
368 forearc region and a clear correlation between the structural heterogeneity and  
369 distribution of large earthquakes occurred in the interpolate thrust zone (Zhao et al.,  
370 2009). The Mw 9.0 Tohoku-Oki earthquake occurred in the interpolate thrust zone and  
371 extends with large coseismic slip in a prominent high-velocity area, that all stress  
372 accumulated on the mainshock asperity may be released in a short time (Huang and  
373 Zhao, 2013) and influenced the tectonic stress field throughout Japan, particularly in  
374 northeastern Japan. The subducting Pacific plate and the overriding continental plate  
375 may become weakly coupled (Zhao et al., 2011). Zhao et al (2011) and Tong et al.  
376 (2012) used P- and S-wave data to obtain high-resolution tomographic images for the  
377 2011 Iwaki earthquake (Mj 7.0) and for the area of the Fukushima nuclear power plant,  
378 their results exhibit that our study area with a high-velocity in the megathrust. Those  
379 3-D P and S wave velocity results (e. g., Zhao et al., 2011; Tong et al., 2012 ) suggest  
380 that the Iwaki earthquake was triggered by ascending fluids from the dehydration of  
381 the Pacific slab and by the stress variation induced by the Tohoku-Oki earthquake,  
382 supporting our results.

### 383 **Acknowledgment**

384 We thank three reviewers and the editor for their helpful comments to improve our  
385 manuscript. This work is co-supported by the State Key Development Program for  
386 Basic Research of China (No. 2013CB733304, 2013CB733303), the National Natural  
387 Science Foundation of China (Nos. 41074007, 41021061 and 41204010), the Doctoral  
388 Fund of Ministry of Education of China (Nos. 20110141130010, 20090141110055),  
389 the Fundamental Research Funds for the Central Universities (Nos. 114035,  
390 201121402020007), the Open Fund of State Key Laboratory of Geodesy and Earth's  
391 Dynamics (No. SKLGED2013-2-6-E), and the Open Research Fund of Key  
392 Laboratory of Geospace Environment and Geodesy, Ministry of Education of China  
393 (No.12-02-07). The ALOS PALSAR data are provided by JAXA through Geohazard  
394 Supersites. All figures are plotted using Generic Mapping Tools (GMT) version 4.5.1.

395

## 396 **References**

- 397 Active Fault and Earthquake Research Center, 2011. Active fault database of Japan.  
398 [http://riodb02.ibase.aist.go.jp/activefault/index\\_e.html?search\\_no=j008&version](http://riodb02.ibase.aist.go.jp/activefault/index_e.html?search_no=j008&version)  
399 [\\_no=1&search\\_mode=020](http://riodb02.ibase.aist.go.jp/activefault/index_e.html?search_no=j008&version)
- 400 Chen, C.W., Zebker, H.A., 2001. Two-dimensional phase unwrapping with use of  
401 statistical models for cost functions in nonlinear optimization. *Journal of the*  
402 *Optical Society of America*, 18, 338–351.
- 403 Clarke, P.J., Paradissis, D., Briole, P., England, P.C., Parsons, B.E., Billiris, H., Veis,  
404 G., Ruegg, J.C., 1997. Geodetic investigation of the 13 May 1995  
405 Kozani-Grevena (Greece) Earthquake. *Geophysical Research Letters*, 24(6),

406 707-710.

407 Evans, E.L., Meade, B.J., 2012. Geodetic imaging of coseismic slip and postseismic  
408 afterslip: Sparsity promoting methods applied to the great Tohoku earthquake.  
409 Geophysical Research Letters, 39, L11314.

410 Farr, M., Rosen, A., Caro, E., 2007. The Shuttle Radar Topography Mission. Reviews  
411 of Geophysics, 45, RG2004.

412 Feng, G.X., Ding, X. L., Li, Z.W., Mi, J., Zhang, L., Omura, M., 2001. Calibration of  
413 InSAR-derived coseismic deformation map associated with the 2011 Mw 9.0  
414 Tohoku-Oki earthquake. IEEE Geoscience and Remote Sensing letters,  
415 9(2):302-306.

416 Freed, A. M., 2005. Earthquake triggering by static, dynamic and postseismic stress  
417 transfer. Annual Review of Earth and Planetary Sciences, 33:335-67.

418 Fujii, Y., Satake, K., Sakai, S., Shinohara, M., Kanazawa, T., 2011. Tsunami source of  
419 the 2011 off the Pacific coast of Tohoku earthquake. Earth Planets and Space, 63,  
420 815–820.

421 Goldstein, R.M., Werner, C.L., 1998. Radar interferometry filtering for geophysical  
422 application. Geophysical Research Letters, 25(21):4035-4038

423 Hanssen, R. F., 2001. Radar Interferometry: Data Interpretation and Error Analysis,  
424 Kluwer Academic Publishers, Dordrecht, 113-130

425 Harris, R.A., 1998. Introduction to special section: stress triggers, stress shadows, and  
426 implications for seismic hazard. Journal of Geophysical Research, 103,  
427 24347-34358

428 Hirose, F., Miyaoka, K., Hayashimoto, N., Yamazaki, T., Nakamura, M., 2011.  
429 Outline of the 2011 off the Pacific coast of Tohoku earthquake (Mw  
430 9.0)-Seismicity: Foreshocks, mainshock, aftershocks, and induced activity. *Earth  
431 Planets and Space*, 63, 513–518.

432 **Huang, Z., Zhao, D., 2013. Mechanism of the 2011 Tohoku-oki earthquake (Mw 9.0)**  
433 **and tsunami: Insight from seismic tomography. *Journal of Asian Earth Sciences*. 70,**  
434 **160-168.**

435 Imanishi, K., Ando, R., Kuwahara, Y., 2012. Unusual shallow normal-faulting  
436 earthquake sequence in compressional northeast Japan activated after the 2011 off  
437 the Pacific coast of Tohoku earthquake. *Geophysical Research Letters*, 39,  
438 L09306.

439 Ishiyama, T., Sato, H., Sugito, N., Echigo, T., Ito, T., Kato, N., Imaizumi, T., 2001.  
440 Tectonic setting of coseismic surface rupture associated with the 2011 Iwaki  
441 earthquake, Japan Geoscience Union 2011 annual meeting, MIS036-P10.

442 Japan Meteorological Agency (JMA), 2004. The Seismological and Volcanological  
443 Bulletin of Japan for January 2004, Tokyo.

444 Kato, A., Sakai, S., Obara, K., 2011. A normal-faulting seismic sequence triggered by  
445 the 2011 off the Pacific coast of Tohoku earthquake: Wholesale stress regime  
446 changes in the upper plate. *Earth Planets and Space*, 63, 745–748.

447 King, G. C. P., R. S. Stein, J. Lin., 1994. Static stress changes and the triggering of  
448 earthquakes. *Bulletin of the Seismological Society of America*, 84(3), 935-953.

449 Kobayashi, T., Tobita, M., Nishimura, T., Suzuki, A., Noguchi, Y., Yamanaka, M.,

450 2011. Crustal deformation map for the 2011 off the Pacific coast of Tohoku  
451 Earthquake, detected by InSAR analysis combined with GEONET data. *Earth*  
452 *Planets and Space*, 63, 621–625.

453 Kobayashi, T., Tobita, M., Nishimura, T., Suzuki, A., Noguchi, Y., Yamanaka, M.,  
454 Miyahara, B., 2012. InSAR-derived crustal deformation and fault models of  
455 normal faulting earthquake (Mj 7.0) in the Fukushima-Hamadori area. *Earth*  
456 *Planets and Space*, 64, 1209–1221

457 Kubo, A., Fukuyama, E., Kawai, H., and Nonomura, K., 2002. NIED seismic moment  
458 tensor catalogue for regional earthquakes around Japan: Quality test and  
459 application. *Tectonophysics*, 356, 23–48.

460 Kubo.K, Yanagisawa.Y, Ymamoto.T, Nakae.S, Takahashi.H, Toshimitsu.S, Sakano.Y,  
461 Miyaji.Y, Takahashi.M, Oono.T, Komazawa.M (2007) Seamless Digital  
462 Geological Map of “Shirakawa”, Geological Survey of Japan.

463 Loveless, J.P., and Meade, B.J., 2011. Spatial correlation of interseismic coupling and  
464 coseismic rupture extent of the 2011 MW = 9.0 Tohoku-oki earthquake.  
465 *Geophysical Research Letters*, 38, L17306.

466 Massonnet, D., Rossi, M., Carmona, C., Adragna, F., Peltzer, G., Feigl, K., Rabaute,  
467 T., 1993. The displacement field of the Landers earthquake mapped by radar  
468 interferometry. *Nature*, 364: 138-142

469 Mizoguchi K., Uehara.S., Ueta. K., 2012. Surface fault ruptures and slip distribution  
470 of the Mw 6.6 11 April 2011 Hamadoori, Fukushima Prefecture, Northeast Japan,  
471 earthquake. *Bulletin of the Seismological Society of America*, 102 (5), 1949-1956.

472 Mooney, W.D., Laske, G., Masters, T.G., 1998. CRUST 5. 1: A global crustal model  
473 at  $5^{\circ} \times 5^{\circ}$ . *Journal of Geophysical Research*, 103: 727–747

474 Okada, Y., 1985. Surface deformation due to shear and tensile faults in a half-space.  
475 *Bulletin of the Seismological Society of America*, 75 (4), 1135-1154.

476 Okada, T., Yoshida, K., Ueki, S., Nakajima, J., Uchida, N., Matsuzawa, T., Umino, N.,  
477 Hasegawa, A., 2011. Shallow inland earthquake in NE Japan possibly triggered  
478 by the 2011 off the Pacific coast of Tohoku Earthquake. *Earth Planets and Space*,  
479 63: 749-754

480 Otsubo, M., Shigematsu, N., Takahashi, M., Azuma, T., Imanishi, K., Ando, R., 2012.  
481 Slickenlines on fault scarps caused by an earthquake in Iwaki-city (Fukushima  
482 Prefecture, Japan) on 11th of April, 2011. *Journal of the Geological Society*  
483 Japan, 118, 3-4.

484 Ryder, I., Rietbrock, A., Kelson, K., Bürgmann, R., Floyd, M., Socquet, A., Vigny, C.,  
485 Carrizo, D., 2011. Large extensional aftershocks in the continental forearc  
486 triggered by the 2010 Maule earthquake, Chile. *Geophysical Journal International*,  
487 188, 879–890.

488 Simons, M., Fialko, Y., Rivera, L., 2002. Coseismic deformation from the 1999 Mw  
489 7.1 Hector Mine, California, earthquake as inferred from InSAR and GPS  
490 observations. *Bulletin of the Seismological Society of America*,  
491 92(4):1390-1402.

492 Stein, R. S., 1999. The role of stress transfer in earthquake occurrence. *Nature*, 402,  
493 606-609.

494 Toda, S., Lin, J., Stein, R.S., 2011. Using the 2011 Mw 9.0 off the Pacific coast of  
495 Tohoku Earthquake to test the Coulomb stress triggering hypothesis and to  
496 calculate faults brought closer to failure. *Earth Planets and Space*, 63:725-730

497 Toda, S., 2011, <http://www.usgsprojects.org/TohokuQuake2011/>

498 Tong, P., Zhao, D., Yang, D, 2012. Tomography of the 2011 Iwaki earthquake (M7.0)  
499 and Fukushima nuclear power plant area. *Solid Earth* 3, 43-51.

500 Townend, J., Zoback, M.D., 2006. Stress, strain, and mountain building in central  
501 Japan, *Journal of Geophysical Research*, 111, B03411.

502 Wang, R., Lorenzo-Martín, F., Roth, F., 2006. PSGRN/PSCMP - A new code for  
503 calculating co- and post-seismic deformation, geoid and gravity changes based on  
504 the viscoelastic-gravitational dislocation theory. *Computational Geosciences*, 32:  
505 527–541

506 Werner. C., Wegmüller, U., Strozzi, T., Wiesmann, A., 2000. GAMMA SAR and  
507 interferometry processing software. ERS ENVISAT Symposium, Gothenburg,  
508 Sweden, 16-20.

509 Wright, T.J., Parsons, B.E., Jackson, J.A., Haynes, M., Fielding, E.J., England, P.C.,  
510 Clarke, P.J., 1999. Source parameters of the 1 October 1995 Dinar (Turkey)  
511 earthquake from SAR interferometry and seismic body wave modelling. *Earth  
512 and Planetary Science Letters*, 172, 23-37.

513 Xu, C.J., Wang, J.J., Li, Z.H., Drummond, J., 2010. Applying the Coulomb failure  
514 function with an optimally oriented plane to the 2008 Mw 7.9 Wenchuan  
515 earthquake triggering. *Tectonophys*, 491, 119-126.

516 Xu, C.J., He, P., Wen, Y.M., Zhang, L., 2012. Coseismic Deformation and Slip  
517 Distribution for the 2011 Tohoku-Oki Mw 9.0 Earthquake: Constrained by GPS  
518 and InSAR. *Geomatics and Information Science of Wuhan University*, 37(12),  
519 1387-1391

520 Yoshida, K., Hasegawa, A., Okada, T., Inuma, T., Ito, Y. and Asano, Y., 2012. Stress  
521 before and after the 2011 great Tohoku-oki earthquake and induced earthquakes in  
522 inland regions of eastern Japan. *Geophysical Research Letters*, 39, L03302.

523 [Zhao, D., Wang, Z., Umino, N., Hasegawa, A., 2009. Mapping the mantle wedge and  
524 interplate thrust zone of the northeast Japan arc. \*Tectonophysics\* 467, 89-106.](#)

525 [Zhao, D., Huang, Z., Umino, N., Hasegawa, A., Kanamori H., 2011. Structural  
526 heterogeneity in the megathrust zone and mechanism of the 2011 Tohoku-oki  
527 earthquake \(Mw 9.0\). \*Geophys. Res. Lett.\* 38, L17308.](#)

528 Zoback, M. L., 1992. First- and second-order patterns of stress in the lithosphere: The  
529 world stress map project. *Journal of Geophysical Research.*, 97, 11,703–11,728.

530 **Tab captions**

531 Tab. 1 Interferometry pairs used in this study

532 Tab. 2 The source parameters from our study and CMT solution

533 Tab. 3 multilayered crustal model parameters

534

535 **Figure captions**

536 Fig. 1 Earthquakes that occurred in the study region during the PALSAR data

537 acquisition period. (a) The location of overlapping PALSAR data. (b) The earthquakes

538 that occurred between 2011/3/3 and 2011/4/18 in the Track 403 overlap region. (c)

539 The focal depth statistics for the earthquakes in (b). (d) The earthquakes that occurred

540 between 2011/2/2 and 2011/3/20 in the Track 404 overlap region. (e) The focal depth

541 statistics for the earthquakes in (d).

542 Fig. 2 (a) The differential interferogram, (b) the calibration interferogram and (c) the

543 azimuth offset for T403. (d) The differential interferogram, (e) the calibration

544 interferogram and (f) the azimuth offset for T404. The yellow squares indicate the

545 GPS stations. (one fringe represents 11.8 cm of deformation in all interferograms)

546 Fig. 3 The modeled interferograms and their residuals for the uniform-slip model for

547 Track T403 ((a) and (b), respectively) and Track T404 ((c) and (d), respectively).

548 Fig. 4 The inverted slip distributions and their estimated errors for the Itozawa Fault

549 plane in the Iwaki region ((a) and (d), respectively), for the Yunotake Fault plane in the

550 Iwaki region ((b) and (e), respectively), and for the single fault plane in the

551 Kita-Ibarake region ((c) and (f), respectively).

552 Fig. 5 The modeled interferograms and their residuals for the distributed-slip model

553 for Track T403 ((a) and (b), respectively) and for Track T404 ((c) and (d),  
554 respectively).

555 Fig. 6 (a) The static Coulomb stress changes induced by the Mw 9.0 Tohoku-Oki  
556 earthquake and resolved on receiver faults parallel to the main fault and (b) those  
557 provided by Toda (2011) at depths of 20 km. The black dots represent all aftershocks  
558 with magnitudes ranging from 0.1 to 7 between 3/11/2011 and 7/15/2011.

559 Fig. 7 The Coulomb stress changes on different fault planes. (a) The Itozawa Fault  
560 plane in the Iwaki region. (b) The Yunotake Fault plane in the Iwaki region. (c) The  
561 single fault plane in the Kita-Ibarake region.



23 multilayered elastic half-space, which indicates that the maximum slips for the two  
24 earthquakes are 3.28 m and 0.98 m, respectively. The Coulomb stress changes were  
25 calculated for the faults following the 2011 Mw 9.0 Tohoku-Oki earthquake based on  
26 the modeled slip along the fault planes. The resulting Coulomb stress changes indicate  
27 that the stresses on the faults increased by up to 1.1 MPa and 0.7 MPa in the Iwaki and  
28 Kita-Ibarake regions, respectively, suggesting that the Tohoku-Oki earthquake  
29 triggered the two aftershocks, supporting the results of seismic tomography.

30 **Key words:** Tohoku-Oki earthquake, InSAR, slip distribution inversion, Coulomb  
31 stress change, aftershock triggering

## 32 **1. Introduction**

33 The Mw 9.0 Tohoku-Oki earthquake (USGS 38.322°N, 142.369°E) occurred on  
34 March 11, 2011, in the Pacific Ocean east of Japan (Fig. 1(a)), where the Pacific plate  
35 subducts beneath Honshu at a rate of ~9 cm/yr (Imanishi et al., 2012). Due to the  
36 release of long-term accumulated stress, it generated a tsunami that caused significant  
37 damage locally in Sendai. Several estimates of the fault slip distribution have been  
38 published (e.g., Fujii et al., 2011; Loveless and Meade, 2011; Yoshida et al., 2012),  
39 indicating a coseismic slip exceeding 30 m over a wide region.

40 The Tohoku-Oki earthquake has caused large variations in the stress field both  
41 near the source and far from the epicenter, causing a significant increase in seismic  
42 activity in the crust of the overriding plate west of the source area (Okada et al., 2011).  
43 Thousands of aftershocks occurred in the first few months following the Tohoku-Oki  
44 earthquake. Two major aftershocks were the Iwaki earthquake (Mj 7.0), which  
45 occurred in a previous seismic gap on April 11, 2011, and was the strongest on-land  
46 aftershock, and the Kita-Ibarake earthquake (Mj 6.0), which occurred on March 19,  
47 2011 (note: Mj is the quick response magnitude and CMT is the centroid-moment  
48 tensor calculated by the Japan Meteorological Agency (JMA); both are reported by the  
49 NEID (<http://www.fnet.bosai.go.jp/event/search.php?LANG=en>)). We aimed to  
50 answer two main questions regarding these large aftershocks. First, what were the  
51 focal mechanisms of the earthquakes? Other than the CMT solution from the NEID,  
52 there is little published information about the slip distributions. Kobayashi et al. (2012)  
53 used InSAR data to detect the Iwaki earthquake. Second, were the two events

54 triggered by the Tohoku-Oki earthquake? Using earthquake catalog data from the JMA  
55 (2004), the Coulomb stress changes on the fault planes of the Iwaki and Kita-Ibarake  
56 earthquakes have been calculated in some studies (e.g., Okada et al., 2011; Toda et al.,  
57 2011; Imanishi et al., 2012).

58 In this study, we used geodetic data (GPS and InSAR) to constrain the location,  
59 geometry and slip distribution of the two earthquakes. Then, we tested whether these  
60 earthquakes were caused by the Tohoku-Oki earthquake.

## 61 **2. Geological background**

62 As located at a plate boundary, earthquakes occur frequently in Japan. After The  
63 Mw 9.0 Tohoku-Oki earthquake there were several  $M \geq 6$  earthquakes occurred inland  
64 and off Japan's western coast in the Japan Sea (Hirose et al., 2011). These aftershocks  
65 included an Mj 7.0 earthquake on April 11, 2011, and nine moderately sized  
66 earthquakes ( $M_j \geq 5.0$ ) after April 18, 2011. Based on seismic waveforms, the focal  
67 mechanism of the largest aftershock in the study region from the JMA indicates that  
68 these earthquakes were normal faulting events. The aftershock depths (Fig. 1(c) and  
69 (e)) indicate that most aftershocks occurred at depths shallower than 20 km. However,  
70 the area of the Iwaki and Kita-Ibarake earthquakes, in Fukushima prefecture,  
71 northeastern Japan, had lower background seismicity before the 2011 Tohoku-Oki  
72 earthquake (Imanishi et al., 2012).

73 The two aftershocks focused on in this study occurred in the western Iwaki city of  
74 Abukuma-sanchi. Metamorphic rocks and Cretaceous strata, granite and epidiorite are  
75 distributed throughout this area, as are forearc deposits with a Tertiary unconformity

76 (Kubo et al. 2007). Previous field investigations indicate that there are active  
77 strike-slip and normal faults, including the Itozawa Fault and the Yunotake Fault,  
78 which have orientations of N10°W strike, 70°W dip and N60°W strike, 60°S dip,  
79 respectively (Active Fault and Earthquake Research Center, 2011). The Mj 7.0 Iwaki  
80 earthquake produced a 14-km-long westward normal-slip rupture on the Itozawa Fault  
81 and a 16-km-long southward normal-slip rupture on the Yunotake Fault. The  
82 northwestern end of the rupture on the Yunotake Fault is ~2.5 km from the  
83 northwestern end of the Itozawa Fault (Mizoguchi et al., 2012). Both faults have  
84 normal fault scarps with offsets of up to 2 m (e.g., Otsubo et al., 2012). The Yunotake  
85 Fault coincides with a ~200-m-high scarp, which is the result of geologically recent  
86 normal faulting or erosion that bounds the Neogene and pre-Neogene rocks (Kubo et  
87 al., 2007). The Itozawa Fault developed within the Gosaisho metamorphic rocks and is  
88 composed of three strands (Mizoguchi et al., 2012). Although both the Yunotake and  
89 Itozawa faults have been recognized as active (Nakata and Imaizumi, 2002), their  
90 paleoseismic histories are poorly understood. This normal faulting is inconsistent with  
91 the present-day regional stress field in northeastern Japan, which is characterized by a  
92 reverse-faulting regime with E-W compression (e.g., Zoback, 1992; Kubo et al., 2002;  
93 Townend and Zoback, 2006). In the northern Kita-Ibarake region, the seismicity  
94 changed drastically from a quiescent stage to an active stage, with no previously  
95 identified active faults.

### 96 **3. InSAR Surface Displacements and Fault Characteristics**

#### 97 *3.1 InSAR analysis*

98           Phased Array type L-band Synthetic Aperture Radar (PALSAR) images from the  
99   Advanced Land Observing Satellite (ALOS) were selected to derive the crustal  
100   deformation field for the study area of the Iwaki and Kita-Ibarake regions (Fig. 1(a)).  
101   The distributions of aftershocks in the study region are shown in Figs. 1(b) and (d) for  
102   the PALSAR data acquisition period. The origin times of  $M_j > 5.0$  earthquakes are  
103   shown in Figs. 1(b) and (d), and there were no large earthquakes ( $M_j > 5.0$ ) prior to the  
104   Mw 9.0 Tohoku-Oki earthquake. The depths of the earthquakes were concentrated at  
105   depths of 2–16 km, as shown in Figs. 1(c) and (e).

106           Two interferometric pairs were constructed from the PALSAR data (Tab. 1). The  
107   SAR data were processed from raw products with the conventional two-pass  
108   differential interferometry approach (Massonnet et al., 1993) using the GAMMA  
109   software package (Werner et al., 2000). To ensure a high signal-to-noise ratio (SNR), a  
110   3:8 multi-look ratio was applied to the PALSAR data in the azimuth and range  
111   directions during processing. The 3-arc second SRTM DEM (Farr et al., 2007) was  
112   used to remove the phase component due to topography. To further reduce the phase  
113   noise and to improve the interferogram quality, a power spectrum filter (Goldstein et  
114   al., 1998) was applied to filter the interferograms. The minimum-cost flow algorithm  
115   (Chen and Zebker, 2001) was adopted to unwrap the differential interferograms. The  
116   geocoded interferograms are shown in Figs. 2(a) and (d) (one fringe represents 11.8  
117   cm of deformation in all interferograms shown in this paper). In the Figs. 2(a) and (d)  
118   show very dense fringes, with nearly 20 fringes in Fig. 2(a) and nearly 10 fringes in  
119   Fig. 2(d).

120 The contributions to the interferograms (Figs. 2(a) and (d)) include the coseismic  
 121 deformation of the Tohoku-Oki earthquake, deformation due to large aftershocks,  
 122 orbital errors, atmosphere delays and a topographic error phase. The atmospheric  
 123 delays and topographic error phase are considered relatively small compared with the  
 124 deformation (e.g., Feng et al., 2011) and are not considered further in this study. The  
 125 phase contributions can be expressed as follows:

$$126 \quad d_{insar} = d_{Mw9.0} + d_{orbit} + d_{deformation} + d_{error}, \quad (1)$$

127 where  $d_{orbit}$  is the orbit error and can be removed by the polynomial method (e.g.,  
 128 Hanssen, 2001);  $d_{Mw9.0}$  and  $d_{deformation}$  are the coseismic and aftershock deformation,  
 129 respectively; and  $d_{error}$  is the white noise. We can interpolate the dense GPS  
 130 observations of coseismic deformation to obtain the InSAR-based coseismic  
 131 deformation  $d_{Mw9.0}$ . Thus, formula (1) can be rewritten as follows:

$$132 \quad d_{deformation} = d_{insar} - d_{orbit} - d_{Mw9.0} - d_{noise} . \quad (2)$$

133 After removing  $d_{Mw9.0}$ , the corrected interferograms are shown in Figs. 2 (b) and (e).  
 134 The corrected interferogram in Fig. 2(b) indicates that the maximum displacement was  
 135 2.1 m in the line-of-sight (LOS) range. Our results are consistent with the field surveys,  
 136 which show that the Iwaki earthquake caused several normal faulting surface ruptures  
 137 and up to 2 m of deformation (Otsubo et al., 2012). The corrected interferogram in Fig.  
 138 2(e) shows up to 0.44 m of deformation in the LOS range, which is in good agreement  
 139 with the ~0.4 m indicated by a previous InSAR study (Kobayashi et al., 2011).

### 140 *3.2 Azimuth offsets*

141 In addition to phase information, SAR images also contain amplitude information,

142 which is a function of the intensity of image backscattering. The deviation between the  
143 surface deformation and the satellite orbit, as well as the amplitude differences of the  
144 SAR image before and after the earthquake, suggests that each pixel has an offset in  
145 the azimuth and range direction. For earthquakes in remote regions and for large  
146 numbers of aftershocks, it is often difficult to obtain accurate field observations of the  
147 surface rupture (Simons et al., 2002), but SAR-based azimuth offsets can be easily  
148 used to determine the surface trace of a seismogenic fault. In this study, the azimuth  
149 offsets were calculated from two accurate registration images along the orbit direction  
150 deviation. The accuracy of the azimuth offset is less than that of the phase observation,  
151 and the mean of the azimuth offset is less sensitive to the surface deformation than to  
152 the coherence coefficient. Therefore, high-quality azimuth offsets can be obtained  
153 even in an incoherent region (such as the high deformation gradient near a fault).  
154 Normally, the azimuth offsets can provide an accurate fault trace. The azimuth offsets  
155 of the interference pairs T403 and T404 are shown in Figs. 2(c) and (f).

156 In Fig. 2(c), the solid red lines show the Itozawa and Yunotake faults from field  
157 observations (Active Fault and Earthquake Research Center, 2011), and the solid green  
158 line shows the corresponding fault traces extracted by the azimuth offsets. A  
159 comparison of the fault traces from the geological field investigations and using the  
160 azimuth offsets shows that the Yunotake Fault trace is well constrained. The absolute  
161 location of the Itozawa Fault trace is uncertain, but its orientation and length are well  
162 constrained. The fault trace extracted using azimuth offsets could be more accurate if  
163 it were integrated with the interferogram. The strike direction and the location of the

164 Itozawa and Yunotake faults can be determined by the azimuth offset method (Tab. 2).

165 As shown in Fig. 2(f), the fault trace cannot be identified using azimuth offsets  
166 for the T404 interferogram pair, and no corresponding seismogenic fault was detected  
167 from field surveys (JMA, 2004). We conclude that the seismogenic fault associated  
168 with this event is a blind fault.

#### 169 **4. Modeling of Fault Parameters**

170 We inverted the InSAR observations (Figs. 2(b) and (e)) for the geometry and slip  
171 distribution of the seismogenic faults responsible for the aftershocks. The  
172 interferograms were down-sampled to decrease the size of the dataset and accelerate  
173 the inversion.

##### 174 *4.1 Uniform-Slip Model*

175 To determine the source mechanism for the aftershocks, InSAR datasets were  
176 modeled with uniform slip on a rectangular dislocation in an elastic half-space (Okada,  
177 1985). Nine fault parameters (longitude, latitude, length, minimum depth, maximum  
178 depth, strike, dip, slip and rake) were determined in this inversion procedure, which  
179 minimizes the misfit between the observations and predicted values using a non-linear,  
180 downhill simplex algorithm with multiple Monte Carlo iterations to avoid local  
181 minima (Clarke et al., 1997; Wright et al., 1999). Although the InSAR data were  
182 processed with precise orbit information, the interferogram still contained residual  
183 orbit errors, so a linear function was applied to the inverted model to estimate the  
184 residual orbit error. The inverted model can be written as follows:

$$185 \quad d_{InSAR} = Gm + \varepsilon, \quad (3)$$

186 where  $d_{InSAR}$  is the InSAR observations,  $G$  is the design matrix,  $m$  is the  
187 parameter dataset, including fault parameters and orbit parameters, and  $\varepsilon$  is the  
188 observation noise. The ultimate goal of the inversion is to optimally fit the model to  
189 the observed data to minimize the objective function.

190 For the Iwaki earthquake, a two-fault model was used to invert the source  
191 mechanism. The fault locations and strike angles were fixed based on the azimuth  
192 offsets and the geological survey. The inverted fault parameters are given in Tab. 2.  
193 The Itozawa and Yunotake faults experienced normal faulting with rake angles of  $88.4^\circ$   
194 and  $73.5^\circ$ , respectively. The motion along these faults was mainly dip-slip with a small  
195 amount of strike-slip motion, and the total seismic moment was  $1.673 \times 10^{19}$  N m (Mw  
196 6.75). There were several Mw 5.5-6.6 earthquakes that occurred during the SAR data  
197 acquisition period; the epicenters of these earthquakes are shown in Fig. 1. Although it  
198 is difficult to identify the deformation caused by individual earthquakes using the  
199 available geodetic data, the deformation indicated by the interferogram in Fig. 2(a) can  
200 be used for an initial estimate. In addition, small earthquakes (Mw<6.0) would not  
201 have produced large surface ruptures, so the deformation in interferogram T403 was  
202 mainly caused by the Mj 7.0 Iwaki earthquake. The dip and rake angles are similar to  
203 the CMT solution but are smaller than that of Kobayashi et al. (2012) (Tab. 2). The  
204 seismic moment is slightly larger than for the CMT solution but smaller than that of  
205 Kobayashi et al. (2012) (Tab. 2).

206 For the Kita-Ibarake earthquake, a one-fault model was used to invert for its  
207 source mechanism. The strike was fixed at  $155^\circ$  based on the interferogram, and the

208 inverted fault parameters are shown in Tab. 2. The rake is  $103.2^\circ$ , which indicates  
209 nearly normal motion. The slip had a significant dip-slip component with a small  
210 amount of strike-slip motion. The minimum depth at which slip occurred was 1.96 km,  
211 indicating that this is a blind fault that caused a small amount of surface deformation,  
212 with no obvious azimuth offsets in Fig. 2(f). The seismic moment was  $2.28 \times 10^{18}$  N m  
213 (Mw 6.17). The dip angle was similar the CMT solution but smaller than that of  
214 Kobayashi et al. (2011) (Tab. 2). This difference can be attributed to the use of two  
215 faults in the Kobayashi et al. (2011) model. The magnitude determined in this study is  
216 larger than that determined by Kobayashi et al. (2011) and that of the CMT, which is  
217 the smallest of the three.

218 The modeled and residual interferograms are shown in Fig. 3. The uniform-slip  
219 model (Figs. 3(a) and (c)) provides a good fit to the observations overall, but there are  
220 1.5 residual fringes on both sides of the fault in the Iwaki region (Fig. 3(b)). This  
221 misfit is mainly due to the sharp deformation gradient and low coherence near the  
222 epicenter. In the Kita-Ibarake region, the residuals are smaller.

#### 223 *4.2 Distributed-Slip Model*

224 To make the model more reliable and to improve the fit to the observations, a  
225 distributed-slip model was used to derive a more detailed slip distribution. For the  
226 Iwaki earthquake model, we extended the Itozawa and Yunotake fault planes to  
227 lengths of 22 km and 24 km, respectively, both with widths of 30 km. Each fault was  
228 divided into 1 km $\times$ 1 km patches. For the Kita-Ibarake earthquake, the fault plane was  
229 extended to a length of 8 km and a width of 24 km. Because only one fault was used to

230 model this earthquake, the fault plane was divided into 0.5 km×0.5 km patches. In the  
231 distributed-slip model, we solved for the slip magnitude and rake on each patch, and  
232 the other geometrical parameters were fixed based on the uniform-slip model so that  
233 the fault slip has a linear relationship with the surface deformation. The best-fitting  
234 amounts of strike-slip and dip-slip motion for each patch were solved within a  
235 least-squares framework.

236 The resulting slip distribution is shown in Fig. 4. For the Iwaki earthquake, the  
237 slip along the Itozawa and Yunotake faults (Figs. 4(a) and (b)) was mainly  
238 concentrated at depths of 0-3 km. The maximum slip of the Yunotake Fault was 2.5 m,  
239 less than the 4.0 m slip of the Itozawa Fault. For the Kita-Ibarake earthquake, the slip  
240 (Fig. 4(c)) was mainly concentrated at depths of 2-12 km, with a maximum slip of 1.5  
241 m. To estimate the precision of the slip distributions, we used the original observations  
242 to create 100 datasets with random errors and calculated the corresponding spatial slip  
243 distributions. Figs. 4(d-f) show that the maximum model errors are 0.3 m, 0.2 m and  
244 0.3 m for the Itozawa, Yunotake, and Kita-Ibarake faults, respectively, which indicates  
245 that the slip distributions are reliable.

246 The interferogram produced by the best-fit distributed-slip model and its  
247 residuals are shown in Fig. 5. The model fits the observations well, and the residual  
248 errors are very small (Fig. 5). The residual distribution is very random, which is  
249 mainly a result of factors such as atmospheric delays and DEM errors.

250 Comparing Fig. 3 with Fig. 5 reveals that the distributed-slip inversion extended  
251 the lengths and widths of the fault planes. The faults were divided into smaller cells.

252 Then, the slip and rake for each cell were determined, thus producing a more detailed  
253 model of each fault, while the uniform-slip model assumed a constant slip distribution  
254 and rake for each fault. Thus, the results in Fig. 5 are better than those in Fig. 3. The  
255 residual interferograms in Figs. 3 and 5 directly reflect the goodness-of-fit of each  
256 model, indicating that the distributed-slip model produces a more realistic deformation  
257 field.

## 258 **5. Coulomb Stress Changes**

259 The Coulomb failure criterion is the core of the Coulomb stress triggering  
260 hypothesis. Coulomb stress changes can be defined as  $\Delta CFF = \Delta\tau + \mu\Delta\sigma$  (King et  
261 al., 1994), where  $\tau$  is the shear stress on the fault (positive in the inferred direction  
262 of slip),  $\sigma$  is the normal stress (positive for fault unclamping), and  $\mu$  is the  
263 apparent friction coefficient. The general hypothesis of Coulomb stress triggering is  
264 that a positive  $\Delta CFF$  promotes failure, and a negative value inhibits failure.

265 The seismogenic fault plane of the Tohoku-Oki earthquake from Xu et al. (2012)  
266 was used to calculate the Coulomb stress changes on different receiving faults. We  
267 adopted the PSGRN/PSCMP software package (Wang et al., 2006) and assumed a  
268 frictional coefficient of 0.4 (e.g., Toda et al., 2011) to calculate the Coulomb stress  
269 change in a multi-layered crust model using the parameters from CRUST 2.0 (Mooney  
270 et al., 1998).

### 271 *5.1 Coseismic Coulomb Stress Changes on a Parallelized Mainshock Fault*

272 For a receiving fault with the same parameters as the source fault of the  
273 Tohoku-Oki earthquake, the coseismic Coulomb stress changes were calculated and

274 are shown in Fig. 6(a) with aftershocks within 20 km. There were fewer aftershocks in  
275 the region of positive Coulomb stress changes, and the area of the inland aftershock  
276 sequence, including the study region, had a negative Coulomb stress change. The  
277 Coulomb stress changes on the mainshock fault were calculated (Fig. 6(b)) using the  
278 receiver fault model of Toda (2001). Comparing Fig. 6(a) with Fig. 6(b) reveals that  
279 the receiver fault model provided by Toda (2011) fits the aftershock distribution much  
280 better than the model using the Tohoku-Oki receiver fault. Because different  
281 aftershocks have different source mechanisms, the calculation based on the spatial  
282 distribution of aftershocks does not provide an accurate Coulomb stress change for  
283 each aftershock. If the source mechanism for an aftershock is available, it can be used  
284 to calculate more accurate Coulomb stress changes.

## 285 *5.2 Coulomb Stress Change on the Aftershock Faults*

286 After inverting for the slip distribution, we computed the Coulomb stress change  
287 on each slip patch (Fig. 7). For the Iwaki earthquake, the Coulomb stress changes were  
288 0.64~0.97 MPa (Fig. 7(a)) on the Itozawa Fault and 0.04~0.2 MPa (Fig. 7(b)) on the  
289 Yunotake Fault. The larger Coulomb stress change on the Itozawa Fault suggests that  
290 the static Coulomb stress imparted by the Tohoku-Oki earthquake mainly triggered the  
291 aftershock on the Itozawa Fault and then triggered the slip along the Yunotake Fault.  
292 For the Kita-Ibarake earthquake, the Coulomb stress change was 0.26~0.65 MPa (Fig.  
293 7(c)), which is consistent with the value of 0.68 MPa calculated by Kobayashi et al.  
294 (2011). In addition, the Coulomb stress change showed a stratified phenomenon (Fig.  
295 7), which is mainly due to the Green's function calculation using a multi-layer crustal

296 model. Our results indicate that the Tohoku-Oki earthquake promoted aftershocks,  
297 which is consistent with result of Toda et al. (2011).

## 298 **6. Discussion and Conclusion**

299 The majority of aftershocks following the Tohoku-Oki earthquake are located  
300 near the plate interface offshore. Moderate-to-large aftershocks at greater depths may  
301 not cause ground motion strong enough to pose a hazard. However, shallower  
302 aftershocks in the upper crust may represent a significant seismic hazard due to small  
303 source-to-site distances and relatively strong ground motions within frequency ranges  
304 of concern for engineered structures (Ryder et al., 2011). The InSAR data presented in  
305 this paper clearly show that surface deformation was caused by two large shallow  
306 normal-faulting crustal aftershocks.

307 For the Iwaki earthquake, the maximum surface displacement was 2.1 m in the  
308 LOS direction, which is consistent with the 2 m displacement found by Otsubo et al.  
309 (2012) in a field survey. The strikes of the Itozawa and Yunotake faults are  $159.4^\circ$  and  
310  $121.5^\circ$ , respectively (Fig. 2(c)). Comparing our results with historical field surveys  
311 shows consistent results for the location of the Yunotake Fault trace and a shift in the  
312 location of the Itozawa Fault. Integrating interferogram data could improve the  
313 reliability of the fault traces extracted from azimuth offsets. The Kita-Ibarake  
314 earthquake produced up to 0.44 m of surface deformation, which is similar to the 0.4  
315 m of deformation from the study by Kobayashi et al. (2011).

316 Interferograms and seismology show that the Iwaki earthquake (Fig. 1(b)) and the  
317 Kita-Ibarake earthquake (Fig. 1(d)) were both shallow normal-faulting earthquakes.

318 Using InSAR observations and azimuth offsets to constrain the model, we inverted the  
319 source parameters for the two faults involved in the Iwaki earthquake: one fault has a  
320 dip of  $56^\circ$  and a rake of  $-88.4^\circ$ , and the second has a dip of  $48.9^\circ$  and a rake of  $-73.5^\circ$ .  
321 These orientations differ from those of Kobayashi et al. (2012), who found dips of  
322  $57.4^\circ$  and  $79.7^\circ$  and rakes of  $-102.3^\circ$  and  $-107.3^\circ$ , respectively, for the two faults. Our  
323 inversion indicates that the magnitude of the Iwaki earthquake was  $M_w$  6.75, larger  
324 than the  $M_w$  6.6 of the CMT solution but smaller than that of Kobayashi et al. (2012).  
325 For the Kita-Ibarake earthquake, we found a fault dip of  $32.8^\circ$ , a rake of  $-103.2^\circ$  and a  
326  $M_w$  of 6.17, which is larger than the  $M_w$  5.8 of the CMT solution. This difference  
327 may arise from the different data sources for the two solutions. The result of the slip  
328 distribution inversion (Fig. 5) indicates that the deformation in the Iwaki region was  
329 caused by slip along the Itozawa and Yunotake faults that caused a large surface  
330 rupture, consistent with field results. In the Kita-Ibarake region, the minimum depth of  
331 the seismogenic fault is  $\sim 2$  km, so there is little surface deformation and thus little  
332 seismic hazard for this type of earthquake.

333 The Coulomb stress changes show that the Tohoku-Oki earthquake promoted the  
334 occurrence of the Iwaki and Kita-Ibarake earthquakes. Many studies of Coulomb  
335 stress change triggering (e.g., Harris, 1998; Stein, 1999; Freed, 2005) have found that  
336 static Coulomb stress changes play an important role in causing aftershocks on  
337 neighboring faults following a larger earthquake (Toda et al., 2011). The Coulomb  
338 stress model (Xu et al., 2010) shows that Coulomb stresses are mainly affected by the  
339 stress tensor, the receiver fault geometry, pore pressures and the friction coefficient.

340 After the Tohoku-Oki earthquake, seismicity changed abruptly throughout inland  
341 Japan. In the study region (Iwaki and Kita-Ibarake), seismicity was non-existent  
342 before the Tohoku-Oki earthquake. Using onshore GPS observations from 298 stations  
343 in the 2 weeks following the Tohoku-Oki earthquake, Evans et al. (2012) suggested  
344 that the afterslip was located almost exclusively down-dip of the coseismic rupture,  
345 with a transition between a depth of 40 to 50 km, indicating the afterslip did not trigger  
346 aftershocks in the study region.

347 By using earthquake catalog data from the JMA (2004), some studies (Okada et  
348 al., 2011; Toda et al., 2011; Yoshida et al., 2012; Imanishi et al., 2012) have focused on  
349 the stress changes in the aftershock region after the Tohoku-Oki earthquake. These  
350 studies have found that stress changes caused by the Tohoku-Oki earthquake triggered  
351 the normal-faulting earthquake sequence at the Ibaraki-Fukushima prefectural border.  
352 This finding conflicts with the inference of Kato et al. (2011), who argued that a  
353 reversal of stresses occurred as a result of the Tohoku-Oki earthquake. Seismic and  
354 geological data are less practical for obtaining accurate fault geometries and the slip  
355 distributions for aftershocks. When imprecise aftershock fault models are used to  
356 determine the receiver fault for Coulomb stress modeling, the results regarding  
357 whether an aftershock was triggered by the mainshock may be questionable. Therefore,  
358 detailed receiver fault parameters are necessary.

359 In this study, Coulomb stress changes were calculated based on detailed  
360 aftershock slip models, and stress increases of nearly 1 MPa were found. Our results  
361 indicate that the Tohoku-Oki earthquake played an important role in triggering

362 aftershocks, in agreement with the arguments of Imanishi et al. (2012). Although  
363 Kobayashi et al. (2012) also used InSAR data to invert the fault parameters of the  
364 Iwake and Kito-Ibarake earthquakes, they determined a steeper dip and larger rake  
365 angle than we found. They found negative  $\Delta CFF$  values in the area and inferred  
366 that static stress changes did not play a role in promoting these earthquakes.

367 For the northeast Japan arc, there exhibit strong lateral heterogeneity under the  
368 forearc region and a clear correlation between the structural heterogeneity and  
369 distribution of large earthquakes occurred in the interpolate thrust zone (Zhao et al.,  
370 2009). The Mw 9.0 Tohoku-Oki earthquake occurred in the interpolate thrust zone and  
371 extends with large coseismic slip in a prominent high-velocity area, that all stress  
372 accumulated on the mainshock asperity may be released in a short time (Huang and  
373 Zhao, 2013) and influenced the tectonic stress field throughout Japan, particularly in  
374 northeastern Japan. The subducting Pacific plate and the overriding continental plate  
375 may become weakly coupled (Zhao et al., 2011). Zhao et al (2011) and Tong et al.  
376 (2012) used P- and S-wave data to obtain high-resolution tomographic images for the  
377 2011 Iwaki earthquake (Mj 7.0) and for the area of the Fukushima nuclear power plant,  
378 their results exhibit that our study area with a high-velocity in the megathrust. Those  
379 3-D P and S wave velocity results (e. g., Zhao et al., 2011; Tong et al., 2012 ) suggest  
380 that the Iwaki earthquake was triggered by ascending fluids from the dehydration of  
381 the Pacific slab and by the stress variation induced by the Tohoku-Oki earthquake,  
382 supporting our results.

### 383 **Acknowledgment**

384 We thank three reviewers and the editor for their helpful comments to improve our  
385 manuscript. This work is co-supported by the State Key Development Program for  
386 Basic Research of China (No. 2013CB733304, 2013CB733303), the National Natural  
387 Science Foundation of China (Nos. 41074007, 41021061 and 41204010), the Doctoral  
388 Fund of Ministry of Education of China (Nos. 20110141130010, 20090141110055),  
389 the Fundamental Research Funds for the Central Universities (Nos. 114035,  
390 201121402020007), the Open Fund of State Key Laboratory of Geodesy and Earth's  
391 Dynamics (No. SKLGED2013-2-6-E), and the Open Research Fund of Key  
392 Laboratory of Geospace Environment and Geodesy, Ministry of Education of China  
393 (No.12-02-07). The ALOS PALSAR data are provided by JAXA through Geohazard  
394 Supersites. All figures are plotted using Generic Mapping Tools (GMT) version 4.5.1.

395

## 396 **References**

- 397 Active Fault and Earthquake Research Center, 2011. Active fault database of Japan.  
398 [http://riodb02.ibase.aist.go.jp/activefault/index\\_e.html?search\\_no=j008&version](http://riodb02.ibase.aist.go.jp/activefault/index_e.html?search_no=j008&version)  
399 [\\_no=1&search\\_mode=020](http://riodb02.ibase.aist.go.jp/activefault/index_e.html?search_no=j008&version)
- 400 Chen, C.W., Zebker, H.A., 2001. Two-dimensional phase unwrapping with use of  
401 statistical models for cost functions in nonlinear optimization. *Journal of the*  
402 *Optical Society of America*, 18, 338–351.
- 403 Clarke, P.J., Paradissis, D., Briole, P., England, P.C., Parsons, B.E., Billiris, H., Veis,  
404 G., Ruegg, J.C., 1997. Geodetic investigation of the 13 May 1995  
405 Kozani-Grevena (Greece) Earthquake. *Geophysical Research Letters*, 24(6),

406 707-710.

407 Evans, E.L., Meade, B.J., 2012. Geodetic imaging of coseismic slip and postseismic  
408 afterslip: Sparsity promoting methods applied to the great Tohoku earthquake.  
409 Geophysical Research Letters, 39, L11314.

410 Farr, M., Rosen, A., Caro, E., 2007. The Shuttle Radar Topography Mission. Reviews  
411 of Geophysics, 45, RG2004.

412 Feng, G.X., Ding, X. L., Li, Z.W., Mi, J., Zhang, L., Omura, M., 2001. Calibration of  
413 InSAR-derived coseismic deformation map associated with the 2011 Mw 9.0  
414 Tohoku-Oki earthquake. IEEE Geoscience and Remote Sensing letters,  
415 9(2):302-306.

416 Freed, A. M., 2005. Earthquake triggering by static, dynamic and postseismic stress  
417 transfer. Annual Review of Earth and Planetary Sciences, 33:335-67.

418 Fujii, Y., Satake, K., Sakai, S., Shinohara, M., Kanazawa, T., 2011. Tsunami source of  
419 the 2011 off the Pacific coast of Tohoku earthquake. Earth Planets and Space, 63,  
420 815–820.

421 Goldstein, R.M., Werner, C.L., 1998. Radar interferometry filtering for geophysical  
422 application. Geophysical Research Letters, 25(21):4035-4038

423 Hanssen, R. F., 2001. Radar Interferometry: Data Interpretation and Error Analysis,  
424 Kluwer Academic Publishers, Dordrecht, 113-130

425 Harris, R.A., 1998. Introduction to special section: stress triggers, stress shadows, and  
426 implications for seismic hazard. Journal of Geophysical Research, 103,  
427 24347-34358

428 Hirose, F., Miyaoka, K., Hayashimoto, N., Yamazaki, T., Nakamura, M., 2011.  
429 Outline of the 2011 off the Pacific coast of Tohoku earthquake (Mw  
430 9.0)-Seismicity: Foreshocks, mainshock, aftershocks, and induced activity. *Earth  
431 Planets and Space*, 63, 513–518.

432 Huang, Z., Zhao, D., 2013. Mechanism of the 2011 Tohoku-oki earthquake (Mw 9.0)  
433 and tsunami: Insight from seismic tomography. *Journal of Asian Earth Sciences*. 70,  
434 160-168.

435 Imanishi, K., Ando, R., Kuwahara, Y., 2012. Unusual shallow normal-faulting  
436 earthquake sequence in compressional northeast Japan activated after the 2011 off  
437 the Pacific coast of Tohoku earthquake. *Geophysical Research Letters*, 39,  
438 L09306.

439 Ishiyama, T., Sato, H., Sugito, N., Echigo, T., Ito, T., Kato, N., Imaizumi, T., 2001.  
440 Tectonic setting of coseismic surface rupture associated with the 2011 Iwaki  
441 earthquake, Japan Geoscience Union 2011 annual meeting, MIS036-P10.

442 Japan Meteorological Agency (JMA), 2004. The Seismological and Volcanological  
443 Bulletin of Japan for January 2004, Tokyo.

444 Kato, A., Sakai, S., Obara, K., 2011. A normal-faulting seismic sequence triggered by  
445 the 2011 off the Pacific coast of Tohoku earthquake: Wholesale stress regime  
446 changes in the upper plate. *Earth Planets and Space*, 63, 745–748.

447 King, G. C. P., R. S. Stein, J. Lin., 1994. Static stress changes and the triggering of  
448 earthquakes. *Bulletin of the Seismological Society of America*, 84(3), 935-953.

449 Kobayashi, T., Tobita, M., Nishimura, T., Suzuki, A., Noguchi, Y., Yamanaka, M.,

450 2011. Crustal deformation map for the 2011 off the Pacific coast of Tohoku  
451 Earthquake, detected by InSAR analysis combined with GEONET data. *Earth*  
452 *Planets and Space*, 63, 621–625.

453 Kobayashi, T., Tobita, M., Nishimura, T., Suzuki, A., Noguchi, Y., Yamanaka, M.,  
454 Miyahara, B., 2012. InSAR-derived crustal deformation and fault models of  
455 normal faulting earthquake (Mj 7.0) in the Fukushima-Hamadori area. *Earth*  
456 *Planets and Space*, 64, 1209–1221

457 Kubo, A., Fukuyama, E., Kawai, H., and Nonomura, K., 2002. NIED seismic moment  
458 tensor catalogue for regional earthquakes around Japan: Quality test and  
459 application. *Tectonophysics*, 356, 23–48.

460 Kubo.K, Yanagisawa.Y, Ymamoto.T, Nakae.S, Takahashi.H, Toshimitsu.S, Sakano.Y,  
461 Miyaji.Y, Takahashi.M, Oono.T, Komazawa.M (2007) Seamless Digital  
462 Geological Map of “Shirakawa”, Geological Survey of Japan.

463 Loveless, J.P., and Meade, B.J., 2011. Spatial correlation of interseismic coupling and  
464 coseismic rupture extent of the 2011 MW = 9.0 Tohoku-oki earthquake.  
465 *Geophysical Research Letters*, 38, L17306.

466 Massonnet, D., Rossi, M., Carmona, C., Adragna, F., Peltzer, G., Feigl, K., Rabaute,  
467 T., 1993. The displacement field of the Landers earthquake mapped by radar  
468 interferometry. *Nature*, 364: 138-142

469 Mizoguchi K., Uehara.S., Ueta. K., 2012. Surface fault ruptures and slip distribution  
470 of the Mw 6.6 11 April 2011 Hamadoori, Fukushima Prefecture, Northeast Japan,  
471 earthquake. *Bulletin of the Seismological Society of America*, 102 (5), 1949-1956.

472 Mooney, W.D., Laske, G., Masters, T.G., 1998. CRUST 5. 1: A global crustal model  
473 at  $5^{\circ} \times 5^{\circ}$ . *Journal of Geophysical Research*, 103: 727–747

474 Okada, Y., 1985. Surface deformation due to shear and tensile faults in a half-space.  
475 *Bulletin of the Seismological Society of America*, 75 (4), 1135-1154.

476 Okada, T., Yoshida, K., Ueki, S., Nakajima, J., Uchida, N., Matsuzawa, T., Umino, N.,  
477 Hasegawa, A., 2011. Shallow inland earthquake in NE Japan possibly triggered  
478 by the 2011 off the Pacific coast of Tohoku Earthquake. *Earth Planets and Space*,  
479 63: 749-754

480 Otsubo, M., Shigematsu, N., Takahashi, M., Azuma, T., Imanishi, K., Ando, R., 2012.  
481 Slickenlines on fault scarps caused by an earthquake in Iwaki-city (Fukushima  
482 Prefecture, Japan) on 11th of April, 2011. *Journal of the Geological Society*  
483 Japan, 118, 3-4.

484 Ryder, I., Rietbrock, A., Kelson, K., Bürgmann, R., Floyd, M., Socquet, A., Vigny, C.,  
485 Carrizo, D., 2011. Large extensional aftershocks in the continental forearc  
486 triggered by the 2010 Maule earthquake, Chile. *Geophysical Journal International*,  
487 188, 879–890.

488 Simons, M., Fialko, Y., Rivera, L., 2002. Coseismic deformation from the 1999 Mw  
489 7.1 Hector Mine, California, earthquake as inferred from InSAR and GPS  
490 observations. *Bulletin of the Seismological Society of America*,  
491 92(4):1390-1402.

492 Stein, R. S., 1999. The role of stress transfer in earthquake occurrence. *Nature*, 402,  
493 606-609.

494 Toda, S., Lin, J., Stein, R.S., 2011. Using the 2011 Mw 9.0 off the Pacific coast of  
495 Tohoku Earthquake to test the Coulomb stress triggering hypothesis and to  
496 calculate faults brought closer to failure. *Earth Planets and Space*, 63:725-730

497 Toda, S., 2011, <http://www.usgsprojects.org/TohokuQuake2011/>

498 Tong, P., Zhao, D., Yang, D, 2012. Tomography of the 2011 Iwaki earthquake (M7.0)  
499 and Fukushima nuclear power plant area. *Solid Earth* 3, 43-51.

500 Townend, J., Zoback, M.D., 2006. Stress, strain, and mountain building in central  
501 Japan, *Journal of Geophysical Research*, 111, B03411.

502 Wang, R., Lorenzo-Martín, F., Roth, F., 2006. PSGRN/PSCMP - A new code for  
503 calculating co- and post-seismic deformation, geoid and gravity changes based on  
504 the viscoelastic-gravitational dislocation theory. *Computational Geosciences*, 32:  
505 527–541

506 Werner. C., Wegmüller, U., Strozzi, T., Wiesmann, A., 2000. GAMMA SAR and  
507 interferometry processing software. ERS ENVISAT Symposium, Gothenburg,  
508 Sweden, 16-20.

509 Wright, T.J., Parsons, B.E., Jackson, J.A., Haynes, M., Fielding, E.J., England, P.C.,  
510 Clarke, P.J., 1999. Source parameters of the 1 October 1995 Dinar (Turkey)  
511 earthquake from SAR interferometry and seismic body wave modelling. *Earth  
512 and Planetary Science Letters*, 172, 23-37.

513 Xu, C.J., Wang, J.J., Li, Z.H., Drummond, J., 2010. Applying the Coulomb failure  
514 function with an optimally oriented plane to the 2008 Mw 7.9 Wenchuan  
515 earthquake triggering. *Tectonophys*, 491, 119-126.

516 Xu, C.J., He, P., Wen, Y.M., Zhang, L., 2012. Coseismic Deformation and Slip  
517 Distribution for the 2011 Tohoku-Oki Mw 9.0 Earthquake: Constrained by GPS  
518 and InSAR. *Geomatics and Information Science of Wuhan University*, 37(12),  
519 1387-1391

520 Yoshida, K., Hasegawa, A., Okada, T., Inuma, T., Ito, Y. and Asano, Y., 2012. Stress  
521 before and after the 2011 great Tohoku-oki earthquake and induced earthquakes in  
522 inland regions of eastern Japan. *Geophysical Research Letters*, 39, L03302.

523 Zhao, D., Wang, Z., Umino, N., Hasegawa, A., 2009. Mapping the mantle wedge and  
524 interplate thrust zone of the northeast Japan arc. *Tectonophysics* 467, 89-106.

525 Zhao, D., Huang, Z., Umino, N., Hasegawa, A., Kanamori H., 2011. Structural  
526 heterogeneity in the megathrust zone and mechanism of the 2011 Tohoku-oki  
527 earthquake (Mw 9.0). *Geophys. Res. Lett.* 38, L17308.

528 Zoback, M. L., 1992. First- and second-order patterns of stress in the lithosphere: The  
529 world stress map project. *Journal of Geophysical Research.*, 97, 11,703–11,728.

530 **Tab captions**

531 Tab. 1 Interferometry pairs used in this study

532 Tab. 2 The source parameters from our study and CMT solution

533 Tab. 3 multilayered crustal model parameters

534

535 **Figure captions**

536 Fig. 1 Earthquakes that occurred in the study region during the PALSAR data

537 acquisition period. (a) The location of overlapping PALSAR data. (b) The earthquakes

538 that occurred between 2011/3/3 and 2011/4/18 in the Track 403 overlap region. (c)

539 The focal depth statistics for the earthquakes in (b). (d) The earthquakes that occurred

540 between 2011/2/2 and 2011/3/20 in the Track 404 overlap region. (e) The focal depth

541 statistics for the earthquakes in (d).

542 Fig. 2 (a) The differential interferogram, (b) the calibration interferogram and (c) the

543 azimuth offset for T403. (d) The differential interferogram, (e) the calibration

544 interferogram and (f) the azimuth offset for T404. The yellow squares indicate the

545 GPS stations. (one fringe represents 11.8 cm of deformation in all interferograms)

546 Fig. 3 The modeled interferograms and their residuals for the uniform-slip model for

547 Track T403 ((a) and (b), respectively) and Track T404 ((c) and (d), respectively).

548 Fig. 4 The inverted slip distributions and their estimated errors for the Itozawa Fault

549 plane in the Iwaki region ((a) and (d), respectively), for the Yunotake Fault plane in the

550 Iwaki region ((b) and (e), respectively), and for the single fault plane in the

551 Kita-Ibarake region ((c) and (f), respectively).

552 Fig. 5 The modeled interferograms and their residuals for the distributed-slip model

553 for Track T403 ((a) and (b), respectively) and for Track T404 ((c) and (d),

554 respectively).

555 Fig. 6 (a) The static Coulomb stress changes induced by the Mw 9.0 Tohoku-Oki

556 earthquake and resolved on receiver faults parallel to the main fault and (b) those

557 provided by Toda (2011) at depths of 20 km. The black dots represent all aftershocks

558 with magnitudes ranging from 0.1 to 7 between 3/11/2011 and 7/15/2011.

559 Fig. 7 The Coulomb stress changes on different fault planes. (a) The Itozawa Fault

560 plane in the Iwaki region. (b) The Yunotake Fault plane in the Iwaki region. (c) The

561 single fault plane in the Kita-Ibarake region.

Figure

[Click here to download high resolution image](#)

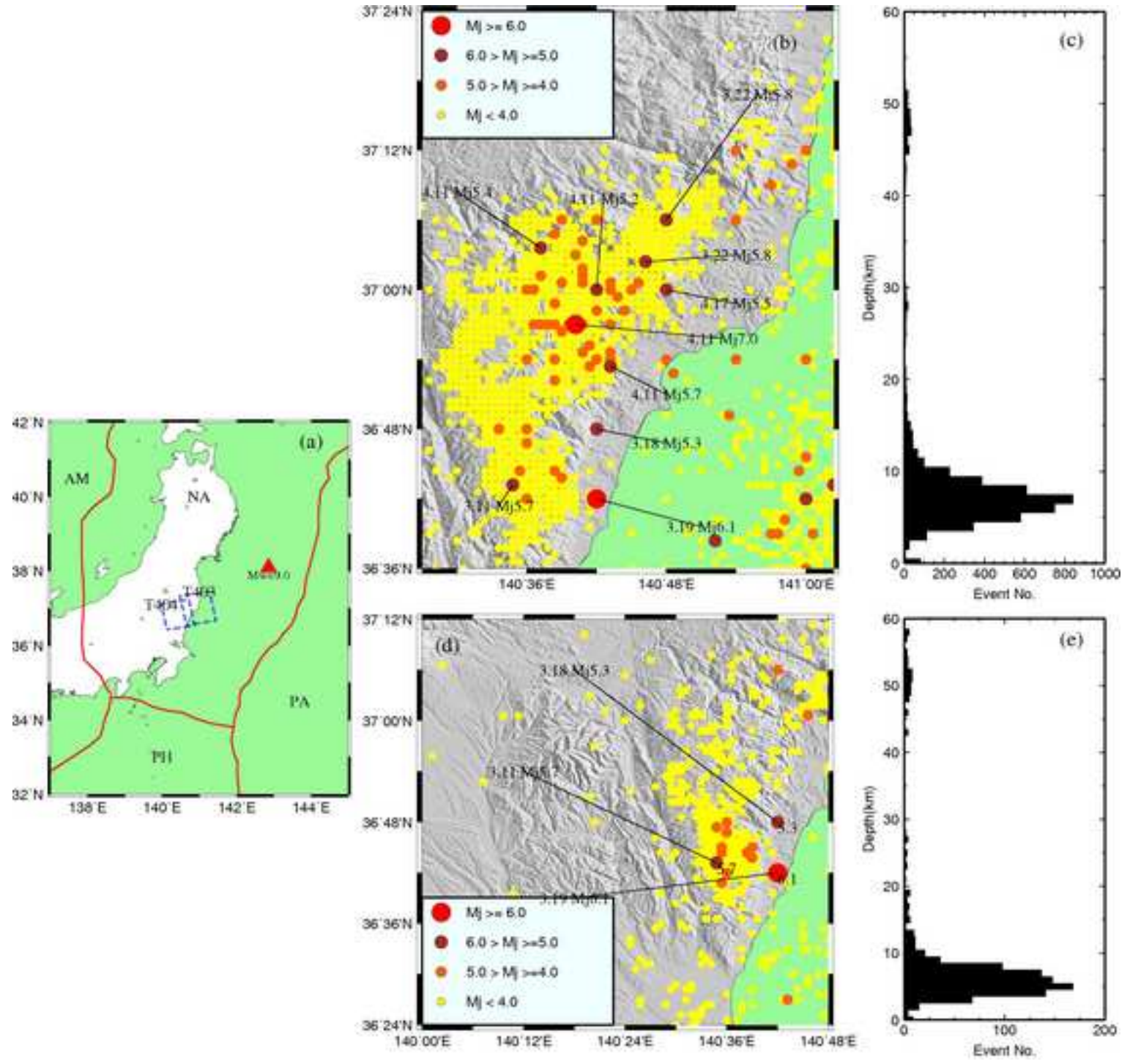


Figure  
[Click here to download high resolution image](#)

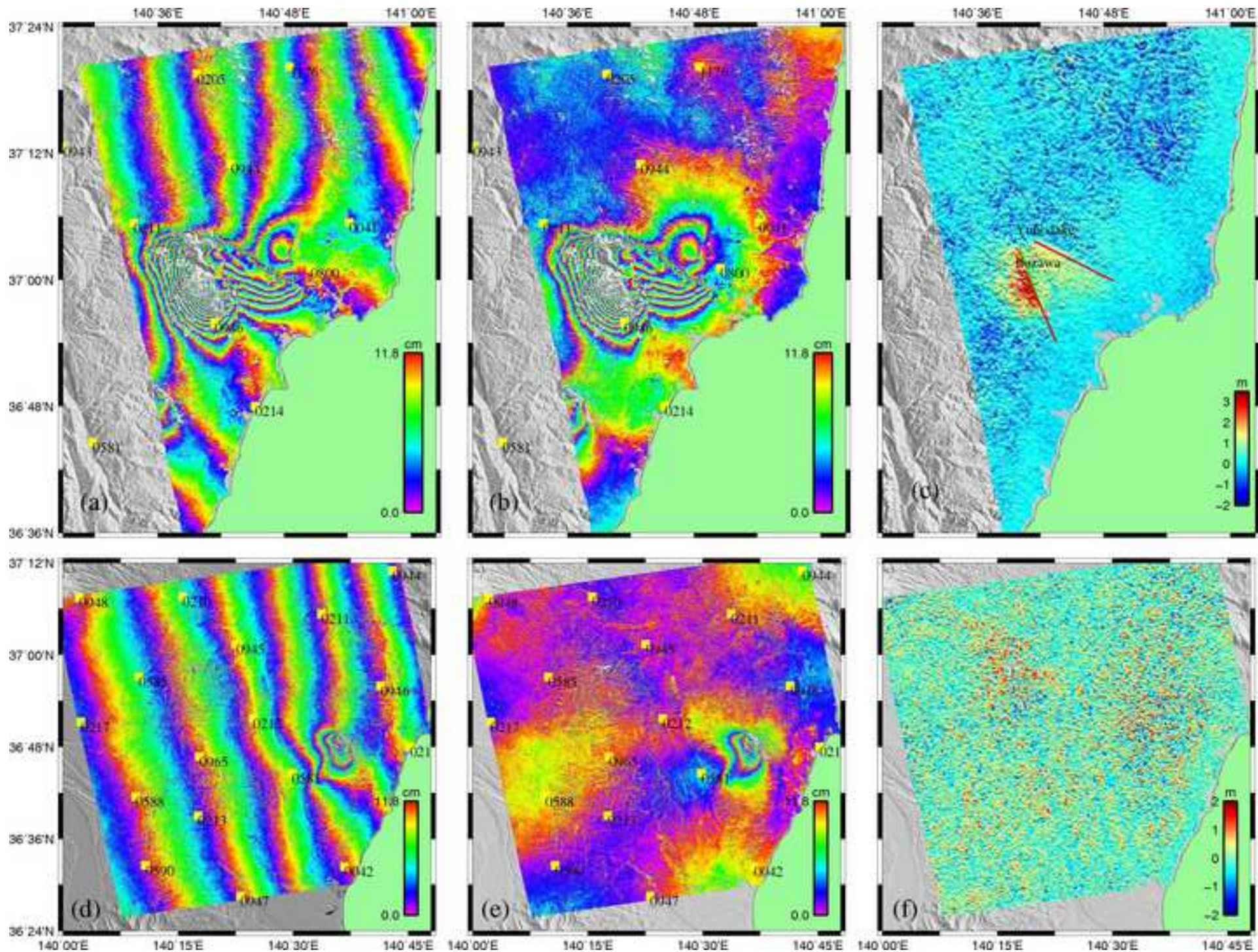
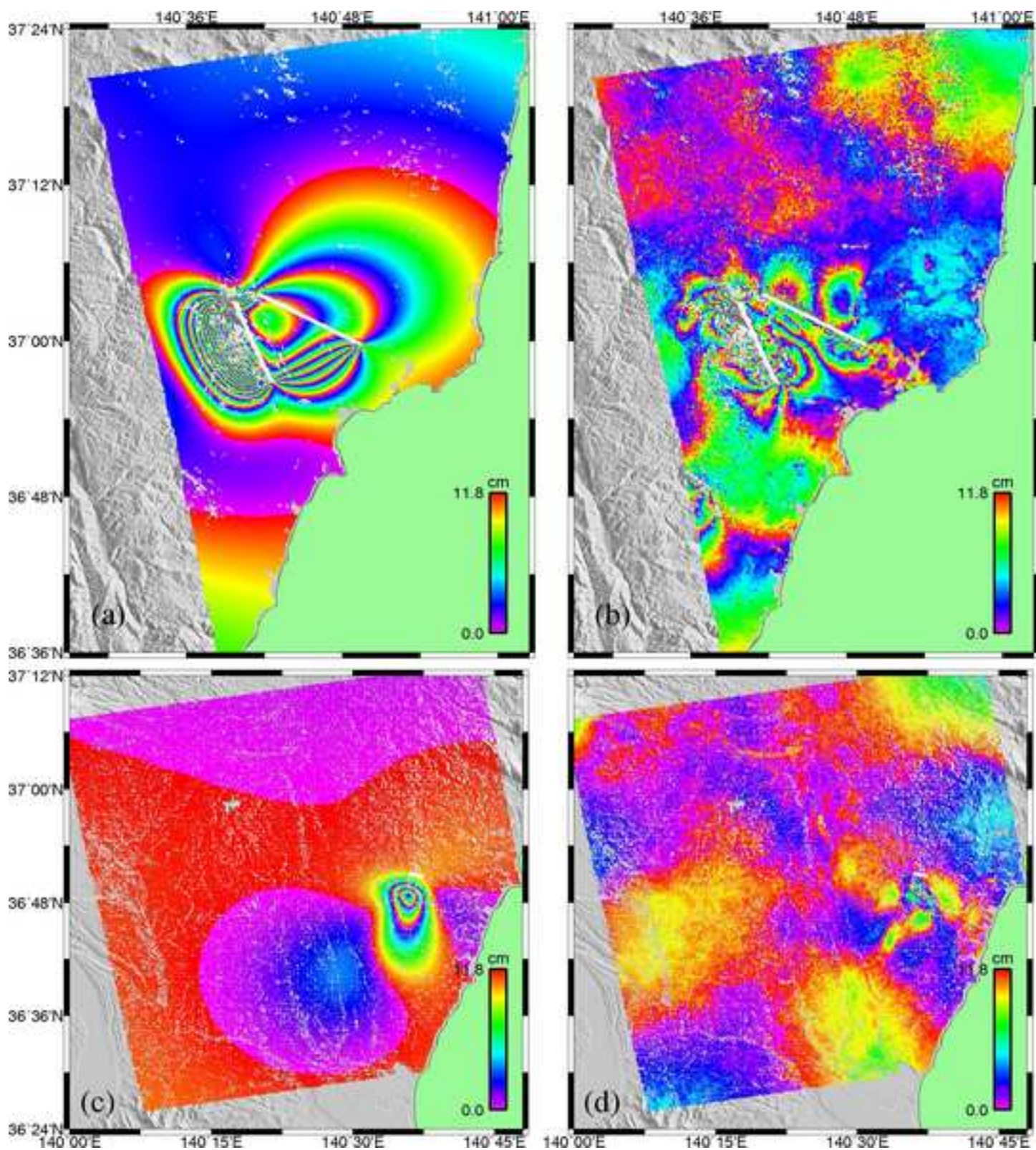


Figure  
[Click here to download high resolution image](#)



Figure

[Click here to download high resolution image](#)

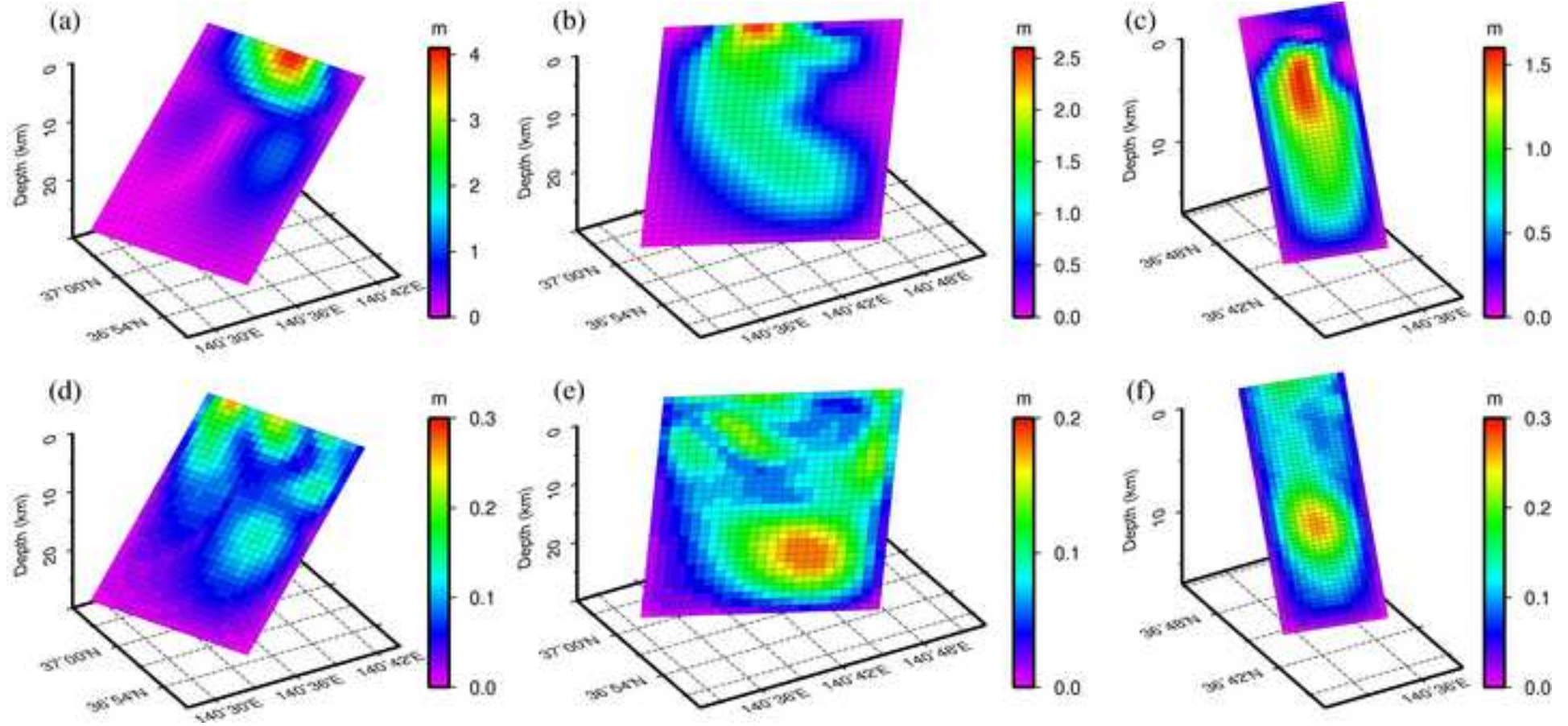


Figure  
[Click here to download high resolution image](#)

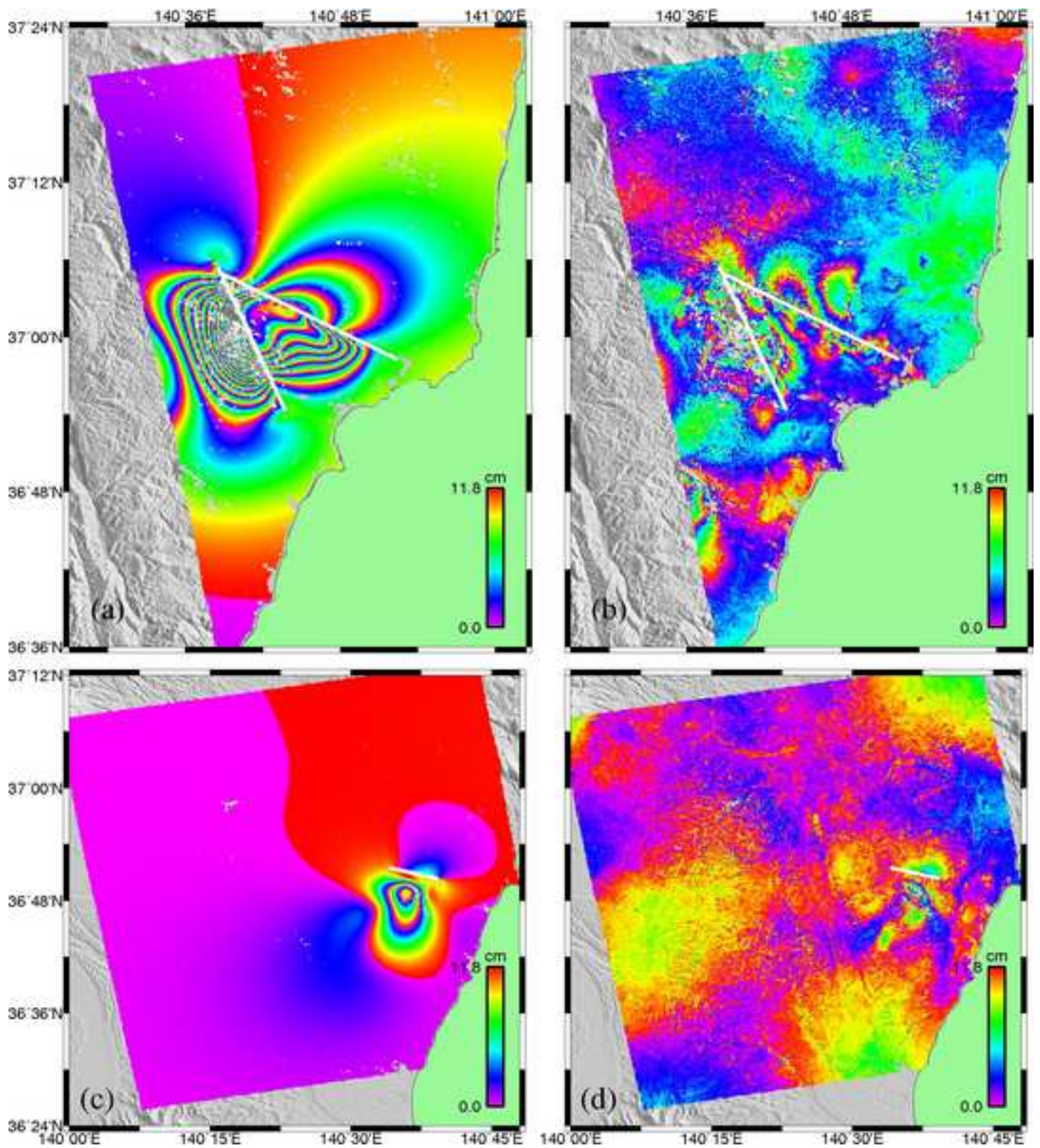
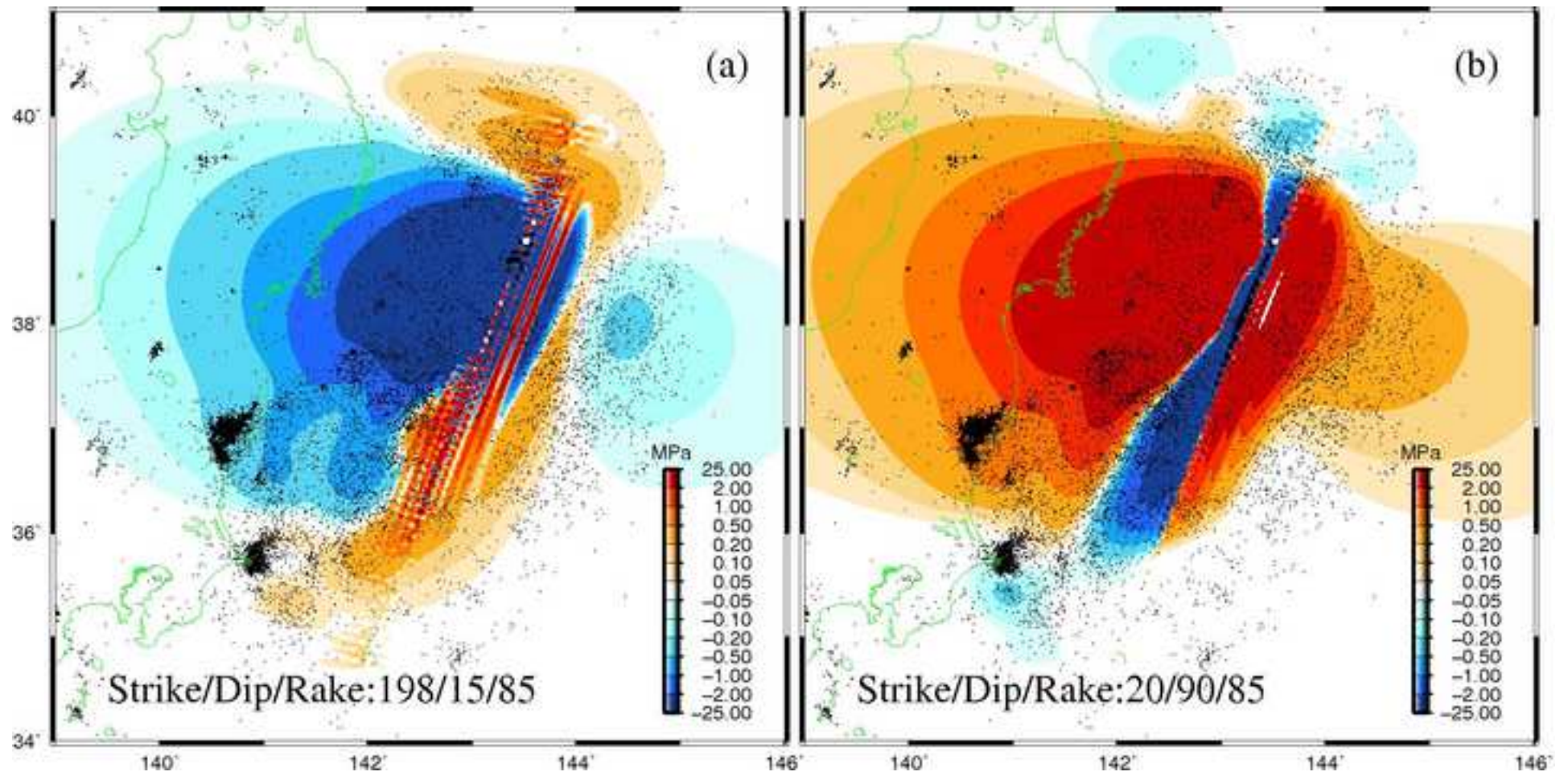
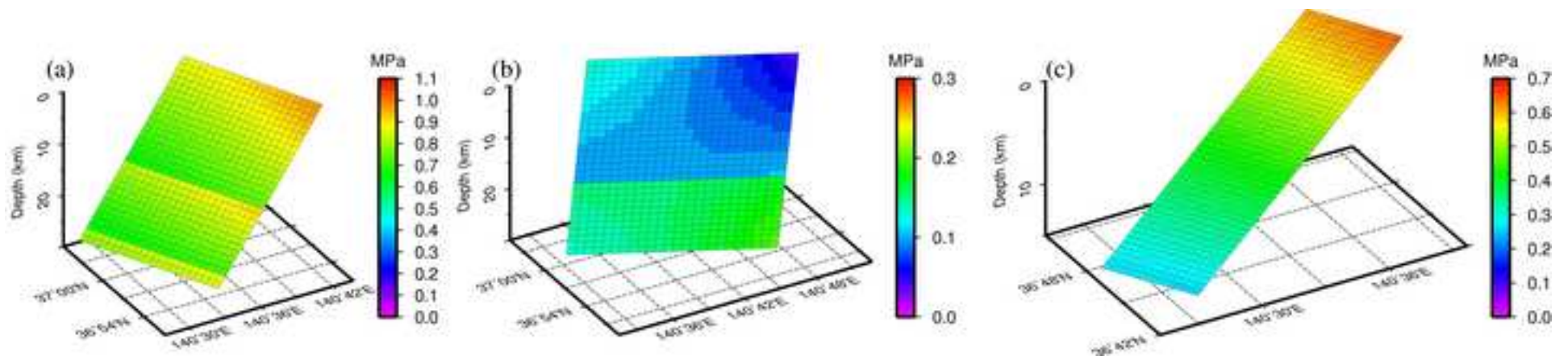


Figure  
[Click here to download high resolution image](#)



# Figure

[Click here to download high resolution image](#)



Tab. 1 Interferometry pairs used in this study

#	Master	Slave	Perp. Baseline(m)	Time span(days)	Track(A/D <sup>†</sup> )	Frame
IP1	110303	110418	347	46	403(A)	2763
IP2	110202	110320	834	46	404(A)	0819

<sup>†</sup> A/D means ascending/descending orbit

1

Tab. 2 The source parameters from different studies

Region	Fault	Lon °	Lat °	Length km	Min Depth km	Max Depth km	Strike °	Dip °	Rake °	Slip m	Moment $10^{18}$ N m	Magnitude Mw
Iwaki (T403)	Itozawa	140.6855	36.9982	12.06	0	5.25	159.4	56	-88.4	3.278	8.00	6.75
		fixed	fixed				fixed					
	Yunotake	140.7585	37.0274	11.59	0	14.93	121.5	48.9	-73.5	1.000	8.73	
		fixed	fixed				fixed					
	Shionohira*	140.667	36.996	11	0	2.9	160	57.4	-102.3	4.1		6.6
Yunotake*	140.743	37.034	14.9	0	4.5	130	79.7	-107.3	1.3		6.4	
	CMT	140.6727	36.9457				132/301	50/41	-82/-99		9.58	6.6
Kita-Ibarake (T404)	InSAR	140.6449	36.8156	7.9517	1.96	7.20	155.00	32.8	-103.2	0.98	2.28	6.17
		fixed					fixed					
	InSAR <sup>†</sup>	140.605	36.793	6.9			157.0	62.5	-107.1	1.5		5.9
		140.609	36.819	2.8			141.6	69.4	-85.7	1.2		5.4
CMT	140.5715	36.7837				141/327	48/42	-94/-86		0.635	5.8	

2 CMT is artificial post-processing report from the JMA, superscript “\*” stands for the results from Kobayashi (2012) and “<sup>†</sup>” stands for the results from Kobayashi  
3 (2011)

Tab. 3 multilayered crustal model parameters

Layer	Depth km	P-wave velocity Km/s	S-wave velocity km/s	Density kg/m <sup>3</sup>
1	0-14	6.0	3.5	2700
2	14-23	6.6	3.7	2900
3	23-34	7.2	4.0	3050
4	>34	8.0	4.6	3100